Evolution of hot fluids in the Chingshui geothermal field inferred from crystal morphology and geochemical data of veins

Yi-Chia Lu[a.], Sheng-Rong Song[a.*], Taguchi Sachihiro[b.], Pei-Ling Wang[c], En-Chao Yeh [d.], Yu-Jie Lin[a], John MacDonald[e.f.], Cédric M. John[e.]

[a] Department of Geosciences, National Taiwan University, Taiwan

[b] Department of Earth System Science, Fukuoka University, Japan

[c] Institute of Oceanography, National Taiwan University, Taiwan

[d] Institute of Earth Sciences, National Taiwan Normal University, Taiwan

[e] Department of Earth Science & Engineering, Imperial College of London, United Kingdom

[f] School of Geographical and Earth Sciences, University of Glasgow, United Kingdom

Abstract

The Chingshui geothermal field once hosted the first geothermal power plant in Taiwan between 1981 to 1993. After a long period of inactivity, this field is attracting renewed interest in order to meet the need for clean energy. A 213-meters length of cores (IC-21) with continuous recovery, the longest in the Chingshui geothermal field, were recovered from 600 m to 813 m below surface in 2010. Three types of calcite crystal morphologies have been identified in veins from the cores of well IC-21: bladed, rhombic and massive crystals. The bladed calcites are generated by degassing in boiling conditions with a precipitation temperature of ~165℃ and calculated $\delta^{18}O$ value of -6.8 ‰ to -10.2 ‰ VSMOW for the thermal water. The rhombic calcites grew in low concentration Ca^{2+} and CO_3^{2-} meteoric fluids and precipitated around ~180℃. Finally, the massive calcites are characterized by co-precipitation with quartz in the mixing zone between meteoric water and magmatic or metamorphic fluids with

calculated $\delta^{18}O$ value up to 1.5±0.7 ‰ VSMOW. Furthermore, the scales and hot fluids at a nearby pilot geothermal power plant confirm a meteoric origin. Based on these observations, we propose that the current orientations of the main conduits for geothermal fluids are oriented N10˚E with a dip 70˚E . This result provides the basic information needed for deploying production and injection wells in future developments of geothermal power plant in this region.

Keywords: Chingshui Geothermal field, clumped isotopes, fluid inclusions, calcite, formation scaling

1. Introduction

Minerals deposited in veins provide important records for studying the evolution of hot fluids in geothermal systems. Isotopic data from fractured-filling carbonate minerals have been found to be particularly useful to constrain the geochemical characteristics of fluid reservoirs and possible post-depositional and syntectonic fluid processes (Iwatsuki et al., 2002; Li et al., 2013; Luetkemeyer et al., 2016; Wallin and Peterman, 1999; Wang et al., 2010). Besides, the crystal morphology, which results from interaction of crystal surfaces and fluids during crystal growth, indicates not only their chemical composition but also the physical parameters relevant to crystallization including temperature, supersaturation, pressure, fluid dynamics and impurities in parent phases (Aquilano et al., 2016). Degassing during boiling is one of the most important factors controlling crystal morphologies in geothermal fields and ore deposits. Many studies have been published that discuss the relationships between

different kinds of crystal morphologies in non-boiling and boiling conditions (Bodnar et al., 1985; Canet et al., 2011; Griffiths et al., 2016; Harvey and Browne, 1992; Moncada et al., 2012; Pei et al., 2017; Simmons and Christenson, 1994; Tulloch, 1982).

The Chingshui geothermal field in northeastern Taiwan (Fig. 1) is an excellent case study for combining both crystal morphology and geochemical data to construct a hydrological model and to estimate fluid evolution in a geothermal system. There are many published geochemical and isotopic data from the hot fluids collected at the pilot geothermal production wells in the field (Chiang et al., 1984; Lin, 2000; Liu et al., 1990, 1982; Yui et al., 1993). The calculated $\delta^{18}O$ values of hot fluids, based on calcite veins from outcrops and cores, were significantly different from that of discharged water from the wells suggesting different sources for the parent fluids of the calcite veins and current geothermal fluids (Lu et al., 2017). It is therefore important to assess conduit orientations and to construct a hydrological model for designing the production and injection wells in the future development of geothermal power plants in the Chingshui geothermal field.

There are 213 meters (depth 600-813m) of continuous core recovered from borehole IC-21, which is the longest core in the Chingshui geothermal field. Abundant calcite veins with different orientations and crystal morphologies were identified and collected for geochemical analyses. In this paper, we use crystal morphologies, isotopic compositions ($\delta^{18}O$ and $\delta^{13}C$ values), and temperatures from fluid inclusions and clumped isotopes of calcites to understand the calcite precipitation conditions in the wells and outcrops, and then to evaluate the parent sources and orientations of fluid conduits in the Chingshui geothermal field. The aim

of this study is to construct a hydrological model for designing the production and injection wells in the future development of geothermal power plants.

2. Background

2.1 Geological setting

The Chingshui geothermal field is located in the Valley of Chingshui River, approximately 13 kilometers southwest of the Ilan Plain, northeast Taiwan (Fig.1). The geothermal field is hosted in argillite/slate of the >3,000 meters-thick Miocene Lushan Formation (Hsiao and Chiang, 1979; Liu et al., 1986; Tseng, 1978). The Lushan Formation has been regarded as a fracture-controlled geothermal reservoir. The meteoric water seeps down through fractures to depth, then is heated to over 200 ℃, and finally flows back to the surface through the fault-controlled conduits (Chen, 1982; Liu et al., 1990, 1982; Yui et al., 1993). Although some researchers have advocated this model (Ho et al., 2014; Hsiao and Chiang, 1979; Lin and Lin, 1995; Lu et al., 2016; Tseng, 1978; Wu and Chiang, 1976), the regional geological structures were mainly inferred from geophysical data due to poor outcrops and are still unclear and controversial (Chang et al., 2014; Hsiao and Chiang, 1979; Su, 1978; Tong et al., 2008).

Two major regional faults named the Xiaonanao fault and Chingshuishi fault, and a few small unnamed ones, cut through rock bodies in this area. The Xiaonanao fault has wide fractured zones and is rich in quartz veins with euhedral crystals along the Chilukeng River, while the Chingshuishi fault was only deduced from geophysical data. Several researchers correlated the fractured zones in the Chilukeng River with

98 the gouges at the Hanshi River and viewed the Xiaonanao fault as a south-dipping
99 thrust associated with Plio-Pleistocene Orogeny (Hsiao and Chiang, 1979; Tseng,
100 1978). Meanwhile, other researchers suggested that there was a third fault cutting
101 through the Chingshui geothermal field, named ‘G fault,' based on fracture
102 distributions from drilling and geophysical data (Huang and Chuang, 1986) (Fig.1).
103 Lu et al. (2017) reported a series of north-dipping small normal faults with strike-slip
104 parallel to the Xiaonanao fault, which are associated with abundant calcite veins
105 (square in Fig.1). These observations imply that the normal faults might be associated
106 with the latest phase of the Okinawa Trough opening (Kimura, 1985).

107 Thermal structure and hydrological circulation of the Chingshui field are still
108 controversial. Lee et al. (2012) proposed cold water recharge from higher altitude
109 anticline fractures to the south, and heated by high geothermal gradient, finally
110 upwelling along the Chingshuishi and G faults. However, Chang et al. (2014) reported
111 that the Chingshuishi Fault and the smaller faults with south dipping parallel to the
112 Xiaonanao fault that are hypothesized to act as water infiltrating fractures are in fact
113 an upwelling permeable zone as demonstrated by magnetotelluric Surveys (MT).

114 2.2 Hydrological background

115 In the Chingshui geothermal field, the hot water is characterized by a high
116 concentration of HCO_3^- (up to 2,768 ppm) and low Cl^- (lower than 40 ppm) with pH
117 values between 8.5 and 9.0, and the non-condensable gasses being predominantly
118 composed of CO_2 (up to 98%) (Lin, 2000) (Table 1). Under these conditions,
119 carbonates would have been precipitated easily when the geothermal reservoir was
120 opened by tectonic activity or drilling for geothermal exploitation. The CO_2 is
121 oversaturated and released quickly by depressurization causing rapid bicarbonate
122 oversaturation with pH increase leading to rapid precipitation of carbonate minerals.

123 There is abundant scaling inside the wells and pipelines which precipitated during
124 power production in this area, and was also interpreted by simulation using the
125 TOUGH2 code (Zhang et al., 2015).

126 2.3 Overview of the pilot Chingshui geothermal power plant

127 A reconnaissance survey of this geothermal field was performed by the Industrial
128 Technology Research Institute (ITRI) from 1973 to 1975 (Lee, 1994). Further
129 exploration was subsequently conducted by the Taiwan Chinese Petroleum
130 Corporation (CPC), and then a 3 MW pilot geothermal power plant was constructed in
131 the field by the National Science Council (NSC) in 1981. It had been operated for
132 12.5 years and then was shut down due to a rapid decline in power production, which
133 was caused by widespread scaling in production pipes (Lin, 2000; Lu et al., 2011).

134 In 2005, the Bureau of Energy of Taiwan restarted geothermal exploration in
135 Taiwan and proposed a plan to develop geothermal energy for future power
136 generation in the Chingshui geothermal field. The Ministry of Science and
137 Technology (MOST) (formerly the National Science Council, NSC) of Taiwan has
138 initiated and promoted geothermal exploration and development as Major National
139 Energy Projects (NEP I & II) since 2008. The works include more precise geological,
140 geochemical and geophysical surveys with drilling (Song, 2012). A 1,158-meter deep
141 production well, named IC-21, was drilled into the reservoir of argillite/slate host
142 rocks. Continuous core 213 m long, between 600 m to 813 m depth, was retrieved in
143 2010.

144 A brand new power plant is to be constructed in the geothermal field. The Ilan
145 County Government initiated a ROT (Rent-Operate-Transfer) project for the
146 Chingshui geothermal power plant in 2016 due to Taiwan’s growing needs for clean

and renewable energy. According to the contract, this plant should have at least 1MW power generation in 2020 and over 3MW in 2022. A hydrological model, thus, is an important and emergent task for deploying the production and injection wells in this region.

3. Samplings and Analytical Methods

3.1 Core descriptions and sample information

A total of 87 carbonate veins in cores from 600-813 meters depth in the IC-21 well were sampled for analysis. The vein information including depths, minerals, and relative orientations were obtained (APPENDIX A. SUPPLEMENTARY DATA 1). The relative orientations of veins were recorded respectively to the dip direction of slaty cleavage in the core. Assuming that the orientations of slaty cleavages at depth are the same to that of the surface, we can re-orient the veins to a true geographic orientation. Two sets of slaty cleavages were observed at the surface nearby the IC-21 drilling site (APPENDIX A. SUPPLEMENTARY DATA 2). The averages of two measurements in cleavages orientations of slates are N70˚W with dip 69˚S and N70˚W with dip 70˚S, respectively. Therefore, we assumed the strikes of cleavages in this area is to be N70˚W, and recalculate the vein orientations in the cores.

Crystal morphologies of calcite were observed under a transmitted light optical microscope (OM) and a Scanning Electron Microscope (SEM). Element compositions of calcite were confirmed by Energy-dispersive spectroscopy (EDS) in the Department of Geosciences National Taiwan University. The mineral phases of veins were determined by X-ray diffraction analysis (XRD) at the National Synchrotron Radiation Research Center (NSRRC) in Taiwan.

3.2 Carbon and oxygen isotopic analyses

A subset of 81 samples was selected for carbon and oxygen isotopic analysis. These were conducted using a Thermo Scientific MAT 253 Isotope Ratio Mass Spectrometer (IRMS) at the Institute of Oceanography, National Taiwan University. The isotopic compositions were normalized to the Vienna Pee Dee Belemnite (V-PDB) for $\delta^{13}C$ and the Vienna Standard Mean Ocean Water (V-SMOW) for $\delta^{18}O$. The δ notation is defined as:

$$\delta\ (‰) = [(R_{sample} / R_{standard}) - 1] \times 1000$$

R is the ratio of either $^{13}C/^{12}C$ or $^{18}O/^{16}O$. The analytical precision (1σ), based on replicate analyses of the carbonate standards, were 0.03 ‰ and 0.06 ‰ for carbon and oxygen isotopes, respectively.

3.3 Clumped isotope analysis

Clumped isotope analysis was conducted at the Qatar Stable Isotope Laboratory at Imperial College London. The details of the sample preparations and analytical procedure have been published in Lu et al., (2017) and Kluge et al., (2015). All of the data processing was performed using "Easotope," a software program designed for complex isotope analysis (John and Bowen, 2016). The parameters used for processing the data were followed procedures highlighted in Schauer et al. (2016) and in Daëron et al. (2016) to avoid problems with ^{17}O correction. The calcite precipitation temperature calculated from corrected Δ_{47} values were based on experimental calibrations by Kluge et al. (2015) adapted for the new ^{17}O correction. The $\delta^{18}O$ values of fluids were estimated using the equation by Friedman and O'Neil (1977).

193 The clumped-isotope Δ_{47}-temperature relationship has initially mainly been applied
194 to paleoclimate research (e.g. Daëron et al., 2011; Eiler, 2011; Ghosh et al., 2006;
195 Tripati et al., 2010; Zaarur et al., 2011). However, more and more researchers shift
196 their attention to high-temperature applications (e.g. Bergman et al., 2013; Cruset et
197 al., 2016; Dale et al., 2014; Kele et al., 2015; Luetkemeyer et al., 2016; MacDonald et
198 al., 2016; Shenton et al., 2015; Sumner et al., 2015). Kluge et al. (2015) established a
199 calibration curve between 25˚C and 250˚C using precipitation experiments mixing
200 $CaCl_2$ and $NaHCO_3$ in a pressurized reaction vessel at pressures of up to 80 bars. Lu
201 et al., (2017) calculated a clumped-isotope temperature of 214±16˚C from the IC-13
202 scales of Chingshui geothermal field using the equations of Kluge et al. (2015), which
203 is within error but slightly higher than the well logging temperature ranging from
204 187˚C to 210˚C. Accordingly, the Δ47-T equation calibrated by Kluge et al. (2015) is
205 validating the use of this calibration for the well conditions.

206 The massive calcites are opaque at 100 μm thick under microscopy and it is
207 difficult to determine the formation temperature using fluid inclusions. The clumped
208 isotope temperatures provide useful information for those carbonates which we could
209 not estimate previously using fluid inclusions.

210 3.4 Fluid inclusion thermometry

211 Homogenization temperatures were measured on fluid inclusions in highly
212 transparent calcite and quartz crystals from the veins of the cores at the Fukuoka
213 University of Japan. Doubly polished wafers 100 μm thick were measured on a
214 USGS heating and freezing stage, and the accuracy is within 1 % relative error of the
215 measured temperature based on calibration using the SYN FLINC synthetic fluid

inclusion. The heating rate is about 3℃/min, and slower when it is approaching homogenization temperature.

4. Results

4.1 Orientation, mineral assemblages and crystal morphology of veins

The dominant orientations of IC-21 veins are around N10˚E to N20˚E with a steep dip towards the east. Some veins are oriented S70˚E and S30˚W and dipping to the south and west, respectively. It is difficult to determine the orientations of a small number (9/81) of veins from the IC-21 well due to irregular geometry. More than half of IC-21 veins (56/81) are predominantly composed of pure calcite, while the others (25/81) consist of mixtures of calcite and quartz (APPENDIX A. SUPPLEMENTARY DATA 1).

Three kinds of crystal morphologies of calcites in IC-21 veins have been recognized with naked-eye and microscopic observations: massive, rhombic and bladed (Fig.2). The most common one is massive calcite, which was often co-precipitated with quartz. Mosaic contacts observed under the back-scattered detector SEM images (Fig.3a), which show that the calcite and quartz were precipitated at the same time. Moreover, bent- and thick-twinsare often found in massive calcites (Fig.4a). Occurrences of those massive calcites with quartz are found as kink structures and veins. Their orientations vary from N10˚to 20˚E dominantly (Fig.5a). There are also some massive calcites without co-precipitated quartz, which show opaque appearances and well-developed twin structures with dominated orientations of N10-20˚E in the veins (Fig.5d).

Many macroscopically rhombic calcites infilling vugs (Fig.2b) were identified in the cores. They often occur as crystal clusters without twin structures on the surface of twinned massive calcites (Fig.3b). The main orientations of rhombic calcite crystals are also N10 to 20˚E (Fig.5b).

The macroscopically bladed calcites mainly occur in near-vertical fractures (Fig.2c), and fillings of hydraulic-breccias (Fig.2d) at depth intervals of 627-633 m, 680-681m, 690-692m, 713-714m, and 743-745m, and 760-762m (Fig.6c). Those depths corresponded to depths with lower values on sonic (DT) and resistivity (Res) logs (Fig. 6a) (Liu et al., 2013). The size of these crystals reaches to 8 mm. The microscopically bladed calcites can also be found on the top of veins under SEM (Fig. 3c). It should be noted that the sample R92-3 (the number 92 is the drilling run and the number 3 the section of core) is different to other samples with lattice structures. It is characterized by aggregates of numerous parallel platy crystals (Fig.2e). Detailed descriptions of samples are shown in APPENDIX A. SUPPLEMENTARY DATA 1.

4.2 Carbon and oxygen isotopic analyses

Carbon and oxygen isotopic analyses indicate that calcite veins from the Chingshui outcrops and scaling in geothermal wells IC13 and IC19 have the highest and lowest values recorded from the Chingshui geothermal field. $\delta^{13}C$ values from the Chingshui outcrops range from -1.9 ‰ to -0.3 ‰ while $\delta^{18}O$ values range from 8.3 ‰ to 17.8 ‰ (Fig.7) (Lu et al., 2017). $\delta^{13}C$ values from scaling in wells IC13 and IC19 range from -7.9 ‰ to -7.0 ‰ while $\delta^{18}O$ values range from 2.8 ‰ to 4.86 ‰ (Fig.7) (Lu et al., 2017). Isotopic compositions of calcite veins from the drilled cores of well IC-21 plot between those of Chingshui outcrops and scaling from wells IC13 and IC19, measured by Lu et al., (2017). They range from -6.8 ‰ to -1.5 ‰ and 0.8 ‰ to

14.4 ‰ for $\delta^{13}C$ and $\delta^{18}O$, respectively (APPENDIX A. SUPPLEMENTARY DATA 1, Fig. 7). In detail, most of the rhombic and bladed calcites have more depleted carbon and oxygen isotopic values than those of massive calcite (Fig. 7), ranging from -6.5 ‰ to -3.4 ‰ and 1.8 ‰ to 8.1 ‰ for $\delta^{13}C$ VPDB and $\delta^{18}O$ VSMOW, respectively.

4.3 Clumped isotope analysis

The Δ_{47} values of massive and rhombic calcites collected from IC-21 cores are 0.415±0.001 ‰ and 0.422±0.005 ‰ (±1SE), which translates to clumped isotope temperatures of 208±14℃ and 173±16℃, respectively, using the temperature calibration of Kluge et al. (2015). Accordingly, the calculated $\delta^{18}O$ values of the original thermal water are +1.5±0.7 ‰ and -4.0±1.0 ‰, respectively when using the equation of Friedman and O'Neil (1997) (Table 2).

4.4 Fluid inclusion thermometry

All observed fluid inclusions in calcites and quartz are predominantly composed of two-phase liquid and vapor at room temperature without any daughter minerals (Fig. 8). The homogenization temperatures of rhombic calcites are distributed widely, ranging from 166 ˚C to 235 ˚C, which is higher than that of bladed calcite with temperatures between 152 ˚C and 180 ˚C (Fig. 6e, Table 3). The homogenization temperature of massive calcites is not easy to measure because of their opacity in host crystals, so the co-precipitated quartz sample (R100-1) was measured instead. The quartz recorded homogenization temperatures ranging from 179 ˚C to 254 ˚C (Fig. 4, Table 3).

5. Discussion

285 5.1 Formation of crystal morphology

286 5.1.1. Bladed calcite

287 Bladed calcites with skeletal structures have often been reported in epithermal and
288 geothermal systems (André-Mayer et al. 2002; Canet et al., 2011; Harvey and Browne,
289 1992; Moncada et al., 2012; Pei et al.,2017; Simmons and Christenson, 1994; Tulloch,
290 1982). Simmons and Christenson (1994) first reported evidence of boiling of fluid
291 inclusions by coeval vapor-rich ones and Th-Tm plotted figures. The rapid CO_2 loss
292 caused by boiling triggers a quick crystallization of calcite, favoring the formation of
293 the tabular habit, referred to here as bladed calcite.

294 Macroscopic bladed calcites occur only at a depth shallower than 762 meters of
295 IC-21. These observations suggest that carbon dioxide began to degas from the
296 system at depths shallower than 762m below the surface in the Chingshui geothermal
297 field. The vugs and fractures filled by bladed calcites are almost near-vertical
298 orientations (Fig. 2c). It can be interpreted that the steeply dipping conduits have the
299 highest possibility to connect to the surface, thus promoting rapid boiling. Some
300 bladed calcites have also been found in the matrices of hydraulic breccia (Fig. 2d).
301 This evidence indicates that if the fractures opened suddenly, the pressure drop and
302 degassing occurred quickly to ‘explode’ the host rock and precipitate the bladed
303 calcites immediately.

304 Bladed calcite has also been documented in the Broadlands-Ohaaki geothermal
305 field of the Taupo volcanic zone in New Zealand (Simmons and Christenson, 1994;
306 Tulloch, 1982). The bladed calcite in Broadlands-Ohaaki shows clear series-parallel
307 flake crystals, with cross-sectional zones in each bladed calcite crystal showing
308 alternating layers of fluid inclusion-rich and overgrowth inclusion-free zones. In

309 comparison, in the IC-21 cores from the Chingshui geothermal field, some of the
310 bladed calcites show parallel flake structures (Fig. 3d1), but most of the bladed
311 calcites are elongate plate shapes (Fig. 3d2). All of the fluid inclusions are scattered
312 inside the bladed calcite without connecting to the crystal surface (Fig. 8a). We, thus,
313 identified that all of the fluid inclusions are primary inclusions.

314 In the Chingshui geothermal field, most of the fluid inclusions in the bladed
315 calcites are liquid rich inclusions (Fig. 8a) but show wide range variations of
316 homogenization temperatures. A few vapor-rich inclusions have also been observed
317 (Fig. 8a), which suggest that boiling occurred and resulted in bladed calcite formation.

318 5.1.2. Rhombic calcite

319 The macroscopically rhombic calcite in the IC-21 core is characterized by
320 diamond shaped crystal structure. It grows on the top of massive calcites and fills up
321 in natural vugs in the IC-21 core. No twin structures have been observed in massive
322 calcites to suggest that those crystals were not subjected to any stress effects.

323 Generally, the rhombic calcites preferentially form at lower concentrations of
324 CO_3^- and Ca^{2+} ions as they have the minimal difference in surface potential between
325 crystal faces, resulting in the rhombic morphology (Domingo et al., 2006; Lahann,
326 1978; Moore and Wade, 2013). However, higher concentrations of CO_3^- and Ca^{2+}
327 ions with over-saturation has been detected in the well fluids and the Chingshui river
328 water (Table.1). We, thus, speculate that the meteoric water was heated and mixed by
329 steam derived from deeper hot fluids to precipitate rhombic calcites in the cracks.

330 5.1.3. Massive calcite

331 Massive calcites are the most abundant calcite morphology and are found in kink
332 structures and veins with various orientations in core IC-21. Their occurrences are
333 similar to the calcite veins of outcrops near the Xiaonanao fault (Lu et al. 2017). They
334 appear as milky opaque crystals under optical microscopy with twin structures (Fig3a).
335 Many thick twins (>1μm) with bent twins and twinned twins have been found in
336 massive calcite veins. These are thought to form at temperatures of 150˚C to 300˚C
337 with significant deformation in syn-tectonic events, as proposed by Burkhard (1993)
338 and Ferrill et al. (2004).

339 Meanwhile, some of the massive calcites occurred together with euhedral quartz
340 crystals in the IC-21 veins indicate that a drop in temperature might also have played
341 as important a role as degassing when the hot fluids rose up to shallower depths. We,
342 therefore, propose that the veins consisting of massive calcites with quartz were
343 formed during tectonic activity associated with stress changes. When the hot fluids
344 were injected into the shallower fractures, boiling would occur in the fractures and the
345 calcite and quartz could precipitate simultaneously (Fig.3a).

346 There are also some massive calcites not co-precipitated with quartz but are
347 characterized by well-developed twin structures, which indicate they are formed by
348 rapid degassing related to tectonic activity. Meanwhile, the carbon and oxygen
349 isotopic compositions of those samples are scattered in between two end members of
350 outcrops and scaling (Fig. 7). This evidence suggests that the origin of massive
351 calcites might have multiple processes. The massive calcite without quartz occurs in
352 steeply-dipping fractures, which suggest they are conduits which connect to the
353 surface and therefore induce pressure decrease rather than temperature decrease.
354 Accordingly, the isotopically enriched fluids were injected upwards from depth to

355 rapidly precipitate calcite without quartz. However, those massive calcites with
356 isotopically lighter values and twin structures could be generated from heated
357 meteoric fluids, and subjected to later tectonic activity to form the twin structures.

358 5.2 Crystal forming temperature

359 The IC-21 drilling project suffered from serious well collapse events and left
360 drilling rods inside forever. Therefore, the well temperatures shown in Fig.6b and
361 Fig.6d were measured inside rods (Lee et al., 2016), which can be view as final
362 temperature but without detailed depth temperature correction. Accordingly, the
363 borehole temperatures of IC-04 are used for supplement and comparison (Fig. 6b and
364 6d). Well IC-04 is located less than 20 m from well IC-21, which was the highest
365 production well (~114.3 ton/hour) for the pilot geothermal power plant during 1976 to
366 1993.

367 The homogenization temperatures (T_h) of fluid inclusions and well-logging
368 temperature are shown in Fig.6e. The lowest T_h of bladed calcites, around 165 ˚C, is
369 similar to the measured temperature in well IC-21. However, most of the lowest T_h of
370 rhombic calcites are higher than the present measured temperatures by about 10-20 ˚C
371 (Fig.6d, Table 3).

372 Both the fluid inclusion and clumped-isotope temperatures have been done in the
373 same sample, R76-2. The results show that the lowest T_h and the calculated clumped
374 isotope temperature are 186 ˚C and 173±16℃, respectively, which both are higher
375 than the measured temperature, 160℃. The massive calcites recorded higher
376 temperatures than the well temperature, the T_h of quartz co-precipitated with massive
377 calcite being 179-254℃. Meanwhile, the corresponding clumped isotope temperature
378 of massive calcite is 208±14 ˚C based on the equation of Kluge et al. (2015). Those

data suggest that the bladed calcite has crystallized recently at current geothermal conditions, while the rhombic and massive ones may have precipitated from hotter fluids previously present in the Chingshui geothermal field.

Passey and Henkes (2012) reported that calcite is precipitated from fluids with different susceptibilities of C–O bond reordering which record their crystallization history. The more rapid the cooling rate, the shorter the precipitation time, which is from 10^{-6} to 10^{-2} degrees per annum. This may explain why the lowest T_h is higher than the clumped isotope temperature in sample R76-2. The T_h recorded the temperature of calcite precipitation, while the clumped isotope temperature recorded the cooling process, both of which are higher than presently measured temperature. Those evidence may suggest that the Chingshui geothermal field is on a waning stage of the system.

Conversely, we observe that the parallel platy calcite in sample R92-3 has a much lower T_h than measured present-day well temperature, which is the opposite of our measurements on massive calcites. The lowest T_h and measured temperatures are 152℃ and 162℃, respectively. This reverse temperature relationship suggests that the parallel platy calcite may be precipitated from hot fluids from depth mixed with cold water from nearby shallower fractures. Although we did not have a detailed temperature profile along the depth in IC-21 due to drilling rods broken inside the hole, it can be supported from the temperature logging from IC-4 (Fig. 6b and 6d), which shows a temperature drop of about 5-10℃ in several depth intervals.

5.3 Isotopic data and fluid sources

Two end members of carbonates have been recognized by isotopic data in the Chingshui geothermal field. One is the calcite veins near the series of north-dipping

small normal faults which have enriched $\delta^{13}C$ and $\delta^{18}O$ values ranging from -1.9 ‰ to -0.3 ‰ and 8.3 ‰ to 17.8 ‰, respectively. The other is the scaling in geothermal wells having $\delta^{13}C$ and $\delta^{18}O$ from -7.9 ‰ to -7.0 ‰ VPDB and 2.8 ‰ to 4.86 ‰ VSMOW (Fig.6), respectively. The calculated $\delta^{18}O$ values of fluid are -1.0±1.6 ‰ to 10.0±1.3 ‰ VSMOW from outcropping calcite veins and -5.8±0.8 ‰ VSMOW from scaling in the well (Lu et al., 2017).

According to Lu et al. (2017), those calcite veins with heavy carbonate isotopic values were precipitated from fluid dominant in magmatic or metamorphic origins, wnich show $\delta^{18}O$ values ranging from +5.5 ‰ to +10.0 ‰ and +5 to +25 ‰, respectively (Taylor, 1974). Moreover, The rock formation underneath the Lushan Formation is a pre-Tertiary basement that is predominantly composed of marble (Ernst, 1983). The $\delta^{13}C$ values of this marble range from 0 ‰ to +4.0 ‰ (Chu and Shieh, 1981; Yui and Lan, 1991), which is higher than the local meta-sandstone in the Lushan Formation, which ranges from -3.2 ‰ to -2.5 ‰ (Lu et al., 2017). The decarbonization of marble could result in heavy carbon isotopic values in the magmatic or metamorphic thermal fluids.

The calcite scaling with more depleted carbonate isotope values are formed under meteoric water dominant conditions. The $\delta^{18}O$ value of thermal water and steam from geothermal plant range from -4 ‰ to -6.7 ‰ and -11.6‰ to -8.0‰ VSMOW, respectively (Liu et al., 1990). Those of dissolved inorganic carbon (DIC) in geothermal water range from -8.5 ‰ to -7.5 ‰ (Liu et al., 1982).

Most of the rhombic and bladed calcites have lower carbon and oxygen isotopic values and are closer to the end member of scaling from the pilot geothermal production pipes (Fig. 7). If we calculate the $\delta^{18}O$ value of fluid by $\delta^{18}O$ value of calcite and lowest T_h, the $\delta^{18}O$ value of fluids range from -10.2 to -3.8 ‰ VSMOW

(Table 3). Those values almost overlap in the thermal water and steam of geothermal plant (Liu et al., 1990). Those light $\delta^{18}O$ values indicate that the fluids which precipitated bladed calcite and rhombic calcite may have a meteoric origin with differing amounts of mixing with steam condensed water (Fig. 9).

On the contrary, the $\delta^{13}C$ and $\delta^{18}O$ values of massive calcites are scattered and closer to the end member of veins around the faults in the Chingshui geothermal field. These suggest that the hot water responsible for massive calcite formation comes directly from magmatic or metamorphic fluids or mixing of such fluids with meteoric water in different proportions during polyphase tectonic events.

There are a few datapoints of crystal morphologies and carbonate isotopic values that do not follow the general trends as the aforementioned observations. Sample R53-3 is composed of massive calcite and euhedral quartz with extremely light $\delta^{13}C$ and $\delta^{18}O$ values being -6.8 ‰ VPDB and 0.8 ‰ VSMOW, respectively (Fig.7). Those morphologies with “feathery structures” or “flamboyant structures” on quartz crystal (Fig. 4b) indicate that they are formed during boiling condition of the fluids (Dong and Zhou, 1996; Moncada et al., 2012). The irregular shapes of veins in the sample of R53-3 also suggest that they might be formed at extreme situations with strong degassing and temperature drop due to tectonic activity.

On the contrary, sample R30-1 consists of rhombic calcite with heavy carbon and oxygen isotopic values (Fig.7). Vein orientation of this sample is N70°W with 82°S dip, which is different from the main fluid conduits of N10-20°E. It suggests that a tectonic event with a different stress field orientation may have occurred before the present stress field in the Chingshui area. This event produced the fractures

connecting to the deep reservoir, in which the fluid is characterized by heavy oxygen isotope values (Lu et al., 2017).

5.4 Conduit orientations for thermal fluids

Current thermal fluids for the pilot power plant in the Chingshui geothermal field come from heated meteoric water, which has the most negative $\delta^{18}O$ values of those measured/calculated from Chingshui (Liu et al., 1990, 1982; Lu et al., 2017). They are easily distinguished from hot fluids at depth, which are characterized by heavier oxygen isotope values. Our results indicate that the calcite veins with extremely light δ18O values were precipitated from the heated meteoric water.

Almost all of the veins with bladed and rhombic calcites have relatively light $\delta^{18}O$ values (Fig.7), confirming precipitation from shallow, heated meteoric water. The opened fractures with orientations of N10-20˚E, now filled by calcites with lighter $\delta^{18}O$ values, are the conduits for fluid flowing currently (Fig.10). Moreover, bladed calcites and rhombic calcites occurred at depths with lower sonic (DT) and resistivity (Res) log responses, corresponding with the current fracture system (Fig. 6a).

On the contrary, the veins predominantly composed of massive calcites sometimes associated with quartz may be derived from the fluids of the deep reservoir, which is characterized by the heavier $\delta^{18}O$ and $\delta^{13}C$ values, mixing with shallow meteoric water in different proportions. Those massive calcites may also be precipitated in deeper fractures, and then uplifted to shallow depths. The uplift rate of Chingshui area is around 2-4 mm/yr (Kang et al., 2015). Accordingly, the calcite veins with different crystal morphologies and isotopic ratios from the IC-21 cores may allow us to understand the current conduits of ascending thermal water in the Chingshui geothermal field.

Two sets of conjugate joints have been measured in the field. One is N25-40˚W with dipping 75-90˚E, and N25-30˚E with dipping 75-80˚W, while the other is NE-N10˚E dipping 80-90˚E and N60-70˚W dipping 65-80˚W (Tseng, 1978). The latter is consistent with our measurements from the IC-21 well. Meanwhile, an Anelastic Strain Recovery (ASR) method for in-situ stress measurements on the cores of IC-21 has been done immediately following core recovery. The results show that the current stress state is NE-compression and NW-extension of strike-slip faulting in the Chingshui area (Yeh, et al., 2013). It implies that the cracks with NW orientation must be closed ones, while NE-trending cracks could act as conduits for current fluid flow (Sun and Yeh, 2013; Yeh et al., 2013).

Three possibilities for fault orientations related to the N10-20˚E conduits have been proposed (Fig.11). They are N10-20˚W, N40-50˚E, and co-existing N10-20˚W and N40-50˚E. The orientation of N10-20˚W is consistent with the Chingshuishi fault, while the N40-50˚E coincides with a series of normal faults observed by Lu et al. (2017) (Fig.1). However, there is no strong and decisive evidence to support which fault plays the dominant role at current conduits.

Geochemical tracer tests using tritium were done by the Industrial Technology Research Institute (ITRI) of Taiwan during 2010 to 2011. Tritium tracer was injected into a well located at the most northward site (hole IC-9). Almost no tritium concentrations higher than background were detected (ITRI, 2011). However, sodium benzoate injected at IC-21 could be detected at IC-19, which is located to the north of IC21 (ITRI, 2012). Furthermore, the δD and $\delta^{18}O$ values of geothermal water range from -58 ‰ to -47 ‰ and from -7.4 ‰ to -5.7 ‰, respectively, which are considerably lower, by 20 ‰ in δD, than those of the local river and creek waters. Such results suggest that the recharge area for the thermal water may be located at

500 higher altitude, southeast of the study area (Liu et al., 1990, 1982). We, therefore,
501 suggest that the meteoric water recharging the deep reservoir may come from the SE,
502 an area with higher altitude than the Chingshui geothermal field (Fig.11). On this
503 basis, we recommend that the injection wells should be deployed and drilled in the
504 southeast of this area.

505 5.5 Formation of scaling

506 A 3 MW pilot geothermal power plant was constructed in the Chingshui
507 geothermal field in 1981. After operating for 12.5 years it was shut down due to a
508 major decline in hot fluid production and was considered not economically viable in
509 1993. Much calcite scaling was found inside the pipes, which was likely an important
510 reason for the declining discharge of thermal water. Acidic solutions, therefore, were
511 used to remove the scaling every two years (Lin, 2000). This treatment was useful to
512 increase production, but soon after the re-start of the production, discharging rate
513 decreased over the course of several runs. This result may imply that the scaling
514 formed not only in the pipes but also in the fractures of the reservoir due to the
515 degassing by discharging hot fluids. This could rapidly precipitate bladed calcite and
516 therefore explain why we found many different grain sizes of bladed calcites on the
517 surface of veins under SEM and naked-eye inspection of core IC-21. However, very
518 few calcite veins were found in well IC-04, the first production well in this
519 geothermal field (Huang and Peng, 1976). Additionally, no bladed calcites have been
520 reported at outcrops near IC-04. This suggests that the calcite veins observed in the
521 Chingshui drilled cores may have been precipitated after discharging large amounts of
522 thermal water for power generation.

523 **6. Conclusion**

Three kinds of crystal morphologies of calcite have been recognized in the IC-21 veins: massive, rhombic and bladed calcites. The massive calcite with/without quartz is characterized by opaque milky color and thick twin structures with relatively heavy carbon and oxygen isotopic values and precipitation temperatures higher than 200 ˚C. It tends to form at greater depths via ascending fluids during tectonic activity, generated from the mixing of magmatic or metamorphic fluids and meteoric water in different proportions. The rhombic calcites are transparent and have lighter carbon and oxygen isotopic values, and are interpreted to have precipitated from a fluid dominantly composed of meteoric water with relatively low Ca^{2+} and CO_3^{2-} concentrations during aseismic periods. The bladed calcite with lattice structures indicates that rapid degassing occurred in open cracks connecting to the surface during seismic faulting or the rapid discharging of hot water for the pilot geothermal power plant. The veins in open cracks of N10-20˚E with dip 70˚E may be of heated meteoric water origin as indicated by oxygen isotopic data, which are the same as scaling precipitated by hot fluids in the geothermal power plant. We, therefore, propose that the main orientation of the flow channel is N10-20˚E from south to north. This result provides the basic information to design the production and injection well deploying in near future developments of geothermal power in the Chingshui geothermal field.

Acknowledgements

This work was supported by Ministry of Science and Technology (MOST), Taiwan [MOST 103-3113-M-002-001, MOST 104-3113-M-002-001, and MOST 105-3113-M-002-001]. The authors are grateful to National Synchrotron Radiation Research Center (NSRRC) offered a machine for X-ray Diffraction analysis.

548

549 **Reference**

550 André-Mayer, A.-S., Leroy, J., Bailly, L., Chauvet, A., Marcoux, E., Grancea, L.,
551 Llosa, F., Rosas, J., 2002. Boiling and vertical mineralization zoning: a case
552 study from the Apacheta low-sulfidation epithermal gold-silver deposit,
553 southern Peru. Miner. Depos. 37, 452–464.

554 Aquilano, D., Otálora, F., Pastero, L., García-Ruiz, J.M., 2016. Three study cases of
555 growth morphology in minerals: Halite, calcite and gypsum. Prog. Cryst.
556 Growth Charact. Mater. 62, 227–251. doi:10.1016/j.pcrysgrow.2016.04.012

557 Bergman, S.C., Huntington, K.W., Crider, J.G., 2013. Tracing paleo fluid sources
558 using clumped isotope thermometry of diagenetic cements along the Moab
559 Fault,Utah. Am. J. Sci. 313, 490–515. doi:10.2475/05.2013.03

560 Bodnar R.J.,Reynolds T.J., Kuehn C.A. (1985) Fluid inclusion systematics in
561 epithermal systems.in Society of Economic Geologists, Reviews in Economic
562 Geology,2, Geology and Geochemistry of Epithermal Systems, B.R. Berger
563 and P.M. Bethke, eds., 73-98.

564 Burkhard, M., 1993a. Calcite twins, their geometry, appearance and significance as
565 stress-strain markers and indicators of tectonic regime: a review. J. Struct.
566 Geol. 15, 351–368. doi:10.1016/0191-8141(93)90132-T

567 Burkhard, M., 1993b. Calcite twins, their geometry, appearance and significance as
568 stress-strain markers and indicators of tectonic regime: a review. J. Struct.
569 Geol. 15, 351–368. doi:10.1016/0191-8141(93)90132-T

570 Canet, C., Franco, S.I., Prol-Ledesma, R.M., González-Partida, E., Villanueva-Estrada,
571 R.E., 2011. A model of boiling for fluid inclusion studies: Application to the
572 Bola??os Ag-Au-Pb-Zn epithermal deposit, Western Mexico. J. Geochemical
573 Explor. 110, 118–125. doi:10.1016/j.gexplo.2011.04.005

574 Chang, P.Y., Lo, W., Song, S.R., Ho, K.R., Wu, C.S., Chen, C.S., Lai, Y.C., Chen,
575 H.F., Lu, H.Y., 2014. Evaluating the Chingshui geothermal reservoir in

576 northeast Taiwan with a 3D integrated geophysical visualization model.
577 Geothermics 50, 91–100. doi:10.1016/j.geothermics.2013.09.014

578 Chen, C.S., 1982. A Simple Geological Model For Geothermal Systems In The
579 Central Range of Taiwan. Trans. 3rd Circum-Pacific Energy Miner. Resour.
580 Conf. 393–397.

581 Chiang, S.C., Hu, J.Y., Chen, L.H., 1984. The Isotopic Geochemistry of Water And
582 Carbonate In Chingshui Geothermal Area. Min. Metall. 28, 73–79. (Chinese
583 with English abstract)

584 Chu, J.B., Shieh, Y.N., 1981. Oxygen And Carbon Isotopes And Mineral Chemistry
585 Of Metamorphic Rocks From The Nanao District, Eastern Taiwan. Semin.
586 Plate Tectonics Metamorph. Geol. 583–630.

587 Cruset, D., Cantarero, I., Travé, A., Vergés, J., John, C., 2016. Crestal graben fluid
588 evolution during growth of the Puig-reig anticline (South Pyrenean fold and
589 thrust belt). J. Geodyn. in press. doi:10.1016/j.jog.2016.05.004

590 Daëron, M., Blamart, D., Peral, M., Affek, H.P., 2016. Absolute isotopic abundance
591 ratios and the accuracy of Δ47 measurements. Chem. Geol. 442, 83–96.
592 doi:10.1016/j.chemgeo.2016.08.014

593 Dale, A., John, C.M., Mozley, P.S., Smalley, P.C., Muggeridg, A.H., 2014.
594 Time-capsule concretions: Unlocking burial diagenetic processes in the
595 Mancos Shale using carbonate clumped isotopes. Earth Planet. Sci. Lett. 394,
596 30–37. doi:10.1016/j.epsl.2014.03.004

597 Domingo, C., Loste, E., Garc, J., Fraile, J., 2006. Calcite precipitation by a
598 high-pressure CO_2 carbonation route 36, 202–215.
599 doi:10.1016/j.supflu.2005.06.006

600 Dong, G., Zhou, T., 1996. Zoning in the Carboniferous-Lower Permian Cracow
601 epithermal vein system, central Queensland, Australia. Miner. Depos. 31, 210–
602 224.

603 Eiler, J.M., 2011. Paleoclimate reconstruction using carbonate clumped isotope
604 thermometry. Quat. Sci. Rev. 30, 3575–3588.
605 doi:10.1016/j.quascirev.2011.09.001.

606 Ernst, W.G., 1983. Mineral paragenesis in metamorphic rocks exposed along Tailuko
607 Gorge, Central Mountain Range, Taiwan. J. Metamorph. Geol. 1, 305–329.
608 doi:10.1111/j.1525-1314.1983.tb00277.x

609 Ferrill, D.A., Morris, A.P., Evans, M.A., Burkhard, M., Groshong, R.H., Onasch,
610 C.M., 2004. Calcite twin morphology: A low-temperature deformation
611 geothermometer. J. Struct. Geol. 26, 1521–1529.
612 doi:10.1016/j.jsg.2003.11.028

613 Friedman, I., O'Neil, J.R., 1977. Compilation of stable isotope fractionation factors of
614 geochemical interests, Data of geochemistry, 6th edn. Prof. Paper 440-KK,
615 Washington D.C., KK1–KK12., U. S. Geol. Surv.

616 Griffiths, L., Heap, M.J., Wang, F., Daval, D., Gilg, H.A., Baud, P., Schmittbuhl, J.,
617 Genter, A., 2016. Geothermal implications for fracture-filling hydrothermal
618 precipitation. Geothermics 64, 235–245.
619 doi:10.1016/j.geothermics.2016.06.006

620 Ghosh, P., Adkins, J., Affek, H.P., Balta, B., Guo, W., Schauble, E.A., Schrag, D.,
621 Eiler, J.M., 2006. 13C–18O bonds in carbonate minerals: a new kind of
622 paleothermometer. Geochim. Cosmochim. Acta 70, 1439–1456.
623 doi:10.1016/j.gca.2005.11.014

624 Harvey, C.C., Browne, P.R.L., 1992. Note on the occurence and compositions of
625 calcite from the Te Mihi sector of the Wairakei Geothermal System, New
626 Zealand. Proc. New Zeal. Geotherm. Work. 345–350.

627 Ho, G.R., Chang, P.Y., Lo, W., Liu, C.M., Song, S.R., 2014. New evidence of
628 regional geological structures inferred from reprocessing and resistivity data
629 interpretation in the Chingshui-Sanshing-Hanchi area of Southwestern Ilan
630 County, NE Taiwan. Terr. Atmos. Ocean. Sci. 25, 491–504.
631 doi:10.3319/TAO.2014.01.24.01(TT)

Hsiao, P.T., Chiang, S.C., 1979. Geology and Geothermal System of the Chingshui-Tuchang Geothermal Area, Ilan, Taiwan. Pet. Geol. Taiwan 16, 205–213.

Huang, J.S., Peng, D.H., 1976. Subsurface Geological Report of IC-4 well Ching-Shui, I-Lan. Taiwan Pet. Explor. Div. 1–13. (Chinese content)

Huang, S.T., Chuang, K.C., 1986. Study of alteration minerals and hydrothermal system in Chingshui geothermal field. Pet. Eng. Taiwan 27, 181–210.

ITRI, 2012. Development of Sustainable Technologies for Traditional and Deep Geothermal Energy (3/4). (Chinese content)

ITRI, 2011. Development of Sustainable Technologies for Traditional and Deep Geothermal Energy (2/4). (Chinese content)

Iwatsuki, T., Satake, H., Metcalfe, R., Yoshida, H., Hama, K., 2002. Isotopic and morphological features of fracture calcite from granitic rocks of the Tono area, Japan: A promising palaeohydrogeological tool. Appl. Geochemistry 17, 1241–1257. doi:10.1016/S0883-2927(01)00129-9

John, C.M., Bowen, D., 2016. Community software for challenging isotope analysis: First applications of “Easotope” to clumped isotopes. Rapid Commun. Mass Spectrom. 30, 2285–2300. doi:10.1002/rcm.7720

Kang, C.C., Chang, C.P., Siame, L., Lee, J.C., 2015. Present-day surface deformation and tectonic insights of the extensional Ilan Plain, NE Taiwan. J. Asian Earth Sci. 105, 408–417. doi:10.1016/j.jseaes.2015.02.013

Kele, S., Breitenback, S.F.M., Capezzuoli, E., Meckler, N.A., Ziegler, M., Millan, I.M., Kluge, T., Deak, J., Hanselmann, K., John, C.M., Yan, H., Liu, Z., Bernasconi, S., 2015. Temperature dependence of oxygen- and clumped isotope fractionation in carbonates: a study of travertines and tufas in the 6-95˚C temperature range. Geochim. Cosmochim. Acta 168, 172–192. doi:10.1016/j.gca.2015.06.032

Kimura, M., 1985. Back-arc rifting in the Okinawa Trough. Mar. Pet. Geol. 2, 222–240. doi:10.1016/0264-8172(85)90012-1

661 Kluge, T., John, C.M., Jourdan, A.L., Davis, S., Crawshaw, J., 2015. Laboratory
662 calibration of the calcium carbonate clumped isotope thermometer in the 25–
663 250 °C temperature range. Geochim. Cosmochim. Acta 157, 213–227.
664 doi:10.1016/j.gca.2015.02.028

665 Lahann, R.W., 1978. A chemical model for calcite crystal growth and morphology
666 control. J. Sediment. Res. 48, 337–347.

667 Lee, C.R., Jang, D., Han, Y.L., Wang, C.Y., 2016. Study on Production Test of IC21
668 Well in Chingshui Geothermal Field, Taiwan. Taiwan Min. Q. 68, 1–12.
669 (Chinese content with English abstract)

670 Lee, C.R., 1994. Compilation of the geothermal prospects data in Taiwan during
671 1966-1979. Bur. Energy Rep. 500. (Chinese content)

672 Li, R., Dong, S., Lehrmann, D., Duan, L., 2013. Tectonically driven organic fluid
673 migration in the Dabashan Foreland Belt: Evidenced by geochemistry and
674 geothermometry of vein-filling fibrous calcite with organic inclusions. J. Asian
675 Earth Sci. 75, 202–212. doi:10.1016/j.jseaes.2013.07.026

676 Lin, C.W., Lin, W.H., 1995. Explanatory Text of the Geologic Map of Taiwan
677 Sanshin. Sheet 15, Cent. Geol. Surv. MOEA,Taiwan. (Chinese content)

678 Lin, J.J., 2000. Study on the Geothermal Power Development of Ching-shui at Ilan
679 Prefecture. J. Pet. Mar. 36, 29–37. (Chinese content with English abstract)

680 Liu, K.K., Yui, T.F., Shieh, Y.N., Chiang, S.C., Chen, L.H., Ho, J.Y., 1982. The C H
681 O isotopic study in Chingshui Geothermal Field, Ilan, Academia Sinica
682 Institude of Earth Sciences report. (Chinese content with English abstract)

683 Liu, K.K., Yui, T.F., Shieh, Y.N., Chiang, S.C., Chen, L.H., Ho, J.Y., 1986. Oxygen
684 and Carbon Isotope Studies of Carbonate Minerals from the Deep Well
685 CPC-CS-16T in the Chingshui Geothermal Field, Taiwan. Pet. Geol. Taiwan
686 22, 69–84.

687 Liu, K.K., Yui, T.F., Shieh, Y.N., Chiang, S.C., Chen, L.H., Ho, J.Y., 1990.
688 Hydrogen and oxygen isotope compositions of meteoric and thermal waters

689 from the Chingshui geothermal area, northeastern Taiwan. Proc. Geol. Soc.
690 China 33, 143–165.

691 Liu, C.M., Yeh, E.C., Sun, T.H., Lin, S.T., Song, S.R., 2013. The geothermal
692 phenomena and core description of Chingshui geothermal field. Western
693 Pacific Earth Sciences, Vol.13, 59-80. (Chinese content with English abstract)

694 Lu, Y.C., Song, S.R., Liu, C.M., Yeh, E.C., 2011. Factors controlling the termination
695 of a 3-Mw-pilot power plant in the Chingshui Geothermal Field, Taiwan, in:
696 Geothermal Resources Council Annual Meeting 2011, Geothermal 2011. San
697 Diego, CA, United States, pp. 1195–1199.

698 Lu, Y.C., Song, S.R., Wang, P.L., Wu, C.C., Mii, H.S., MacDonald, J., Shen, C.C.,
699 John, C.M., 2017. Magmatic-like fluid source of the Chingshui geothermal
700 field, NE Taiwan evidenced by carbonate clumped-isotope paleothermometry.
701 J. Asian Earth Sci. doi:10.1016/j.jseaes.2017.03.004

702 Luetkemeyer, P.B., Kirschner, D.., Huntington, K.W., Chester, J.S., Chester, F.M.,
703 Evans, J.P., 2016. Constraints on paleofluid sources using the clumped-isotope
704 thermometry of carbonate veins from the SAFOD (San Andreas Fault
705 Observatory at Depth) borehole. Tectonophysics.
706 doi:10.1016/j.tecto.2016.05.024

707 MacDonald, J., John, C., Girard, J.-P., 2016. Testing clumped isotopes as a reservoir
708 characterisation tool: a comparison with fluid inclusions in a dolomitised
709 sedimentary carbonate reservoir buried to 2-4 km. Geol. Soc. London. doi:in
710 press

711 Moncada, D., Mutchler, S., Nieto, A., Reynolds, T.J., Rimstidt, J.D., Bodnar, R.J.,
712 2012. Mineral textures and fluid inclusion petrography of the epithermal
713 Ag-Au deposits at Guanajuato, Mexico: Application to exploration. J.
714 Geochemical Explor. 114, 20–35. doi:10.1016/j.gexplo.2011.12.001

715 Moore, C.H., Wade, W.J., 2013. Carbonate Diagenesis: Introduction and Tools, in:
716 Carbonate Reservoirs. Elsevier Inc. Chapters , pp. 1–392.

717 Passey, B.H., Henkes, G.A., 2012. Carbonate clumped isotope bond reordering and
718 geospeedometry, Earth Planet. Sci. Lett., 351–352, pp. 223-236.
719 doi.org/10.1016/j.epsl.2012.07.021

720 Pei, Q., Zhang, S., Santosh, M., Cao, H., Zhang, W., Hu, X., Wang, L., 2017.
721 Geochronology, geochemistry, fluid inclusion and C, O and Hf isotope
722 compositions of the Shuitou fluorite deposit, Inner Mongolia, China. Ore Geol.
723 Rev. 83, 174–190. doi:10.1016/j.oregeorev.2016.12.022

724 Røyne, A., K. N. Dalby, and T. Hassenkam (2015), Repulsive hydration forces
725 between calcite surfaces and their effect on the brittle strength of
726 calcite-bearing rocks, Geophys. Res. Lett., 42, 4786–4794,
727 doi:10.1002/2015GL064365.

728 Schauer, A.J., Kelson, J., Saenger, C., Huntington, K.W., 2016. Choice of ^{17}O
729 correction affects clumped isotope ($\Delta 47$) values of CO_2 measured with mass
730 spectrometry. Rapid Commun. Mass Spectrom. doi:10.1002/rcm.7743

731 Schauer, A.J., Kelson, J., Saenger, C., Huntington, K.W., 2016. Choice of ^{17}O
732 correction affects clumped isotope ($\Delta 47$) values of CO_2 measured with mass
733 spectrometry. Rapid Commun. Mass Spectrom. doi:10.1002/rcm.7743

734 Simmons, S.F., Christenson, B.W., 1994. Origins of calcite in a boiling geothermal
735 system. Am. J. Sci. 294, 361–400.

736 Song, S.R., 2012. National Energy Program: The Study of Chingshui Geothermal
737 Field(3/3), National Science Council 2012-Final report (NSC 101-3113-M-002
738 -001). . (Chinese content with English abstract)

739 Su, F., 1978. Resistivity survey in the Chingshui prospect , I-Lan,Taiwan. Pet. Geol.
740 ofTaiwan 15, 255–264.

741 Sumner, K.K., Camp, E.R., Huntington, K.W., Cladouhos, T.T., M., U., 2015. Assessing
742 Fracture Connectivity using Stable and Clumped Isotope Geochemistry of Calcite.
743 Fortieth Work. Geotherm. Reserv. Eng. Stanford Univ.

744 Sun, T.H., Yeh, E.C., 2013. Study of Stress State around the Chinshui Geothermal
745 District of Ilan Area, Taiwan. National Taiwan Normal University. (Chinese
746 content with English abstract)

747 Taylor, H.P., 1974. The application of oxygen and hydrogen isotope studies to
748 problems of hydrothermal alteration and ore deposition. Econ. Geol. 69, 843–
749 883. doi:10.2113/gsecongeo.69.6.843

750 Taylor, S.R., McLennan, S.M., 1995. The geochemical evolution of the continental
751 crust. Rev. Geophys. 33, 241–265. doi:10.1029/95RG00262

752 Tong, L.T., Ouyang, S., Guo, T.R., Lee, C.R., Hu, K.H., Lee, C.L., 2008. Insight into
753 the geothermal structure in Chingshui, Ilan, Taiwan. Terr. Atmos. Ocean. Sci.
754 19, 413–424. doi:10.3319/TAO.2008.19.4.000

755 Tripati, A.K., Eagle, R.A., Thiagarajan, N., Gagnon, A.C., Bauch, H., Halloran, P.R.,
756 Eiler, J.M., 2010. $^{13}C–^{18}O$ isotope signatures and "clumped isotope"
757 thermometry in foraminifera and coccoliths. Geochim. Cosmochim. Acta 74,
758 5697–5717. doi:10.1016/j.gca.2010.07.006

759 Tseng, C.S., 1978. Geology and Geothermal Occurrence of the Chingshui and
760 Tuchang Districts, Ilan. Pet. Geol. Taiwan 15, 11–23. (Chinese content with
761 English abstract)

762 Tulloch, A.J., 1982. Mineralogical observations on carbonate scaling in geothermal
763 wells at Kawerau and Broadlands: New Zealand Geothermal workshop, 4th,
764 Proceedings p. 131-134.

765 Wallin, B., Peterman, Z., 1999. Calcite fracture fillings as indicators of
766 paleohydrology at È spo Laxemar at the A È Hard Rock Laboratory , southern.
767 Appl. Geochemistry 14.

768 Wang, P.L., Wu, J.J., Yeh, E.C., Song, S.R., Chen, Y.G., Lin, L.H., 2010. Isotopic
769 constraints of vein carbonates on fluid sources and processes associated with
770 the ongoing brittle deformation within the accretionary wedge of Taiwan.
771 Terra Nov. 22, 251–256. doi:10.1111/j.1365-3121.2010.00940.x

772 Wu, Y.J., Chang, B.T., 1976. The geology of the Chingshui and Tuchang geothermal
773 area and surrounding region. Min. Technol. 14, 484–489.

774 Yeh, E.C., Sun, T.H., Lin, S.T., Lee, W.C., Lin, W., Wu, Y.M., Wang, T.T., Song,
775 S.R., Lin, W., 2013. Investigation of Relationship between In-Situ Stress and

776 Fluid Conduits from Chinshui Geothermal Area, NE Taiwan, in: AGU Fall
777 Meeting. p. H51D–1218.

778 Yui, T.F., Lan, C.Y., 1991. Isotopic Compositions of Tananao Marble in the Tungao
779 Area. Spec. Publ. Cent. Geol. Surv. 5, 161–171.

780 Yui, T.F., Liu, K.K., Shieh, Y.N., 1993. Stable isotope systematics of argillite/slate
781 from a deep well in the Chingshui geothermal field, Taiwan. Chem. Geol. 103,
782 181–191. doi:10.1016/0009-2541(93)90300-8

783 Zaarur, S., Olack, G., Affek, H.P., 2011. Paleo-environmental implication of clumped
784 isotopes in land snail shells. Geochim. Cosmochim. Acta 75, 6859–6869.
785 doi:10.1016/j.gca.2011.08.044

786 Zhang, K., Lee, B., Ling, L., Wang, Y., Guo, T., Liu, C., Ouyang, S., 2015.
787 Numerical Evaluation for Production Performance of Chingshui Geothermal
788 Reservoir , Taiwan, Proceedings World Geothermal Congress 2015,
789 Melbourne, Australia, 19-25 April 2015, 19–25.

790

791

Fig. 1. (a) The Chingshui geothermal field (red star) is located in the southwest of Ilan Plain, an area formed during back arc extension of the Okinawa Trough. (b) The red dashed box is the main hot water upwelling zone in the Chingshui area. Three major faults, the Xiaonanao, the Chingshuishi, and the G faults, and several subsidiary normal faults with strike-slip components (black box) have been found in this area. The drilled wells, such as IC-04, -09, -13, -16, -19, and -21 are predominantly distributed in a 1.3 km^2 by the Chingshui River.

Fig. 2. Photographs of the calcite morphologies observed in the veins of IC-21 cores: (a) massive, (b) rhombic, (c) bladed calcites in fractures, (d) bladed calcites in breccias, and (e) parallel platy calcite. The diameters of one and ten dollar coins are 2 and 2.6 centimeters for scales.

Fig. 3. Scanning electron microscopy (SEM) images of calcite morphologies observed in the veins of IC-21 cores: (a) massive, (b) rhombic, (c) bladed calcites on the surface of rhombic calcite, and (d) cross-section view of bladed calcite. (d1) bladed calcites with series-parallel flake crystals, and (d2) bladed calcites are one-layer platy shapes.

Fig. 4. (a) Photomicrograph of massive twinned calcites intergrown with quartz. Yellow arrows denote bent twins. Blue arrows indicate thick twins with twinned twins. (b) Photomicrograph showing feathery structures in sample R53-3, denoted by the yellow arrows.

Fig. 5. Vein orientations in lower hemisphere projections show that veins of N10−20°E with steep inclinations are widely distributed in all crystal morphologies. Orientations of massive calcites with quartz (a) and without quartz (d) have wider variations than that of rhombic calcite crystals (b) and bladed calcites (c).

Fig. 6. (a) The sonic logging (DT) and resistivity (Res) in IC-21 (Liu et al., 2013). (b) The geothermal gradient of IC-04 borehole temperature (light blue to dark blue are 8 hours, 24 and 48 hours after drilling) and the temperature inside the drilling pipe of IC-21(Gray), respectively. (c) The bladed calcites appeared shallower than 762 m in depth of the IC-21. (d) The plot of oxygen isotopes vs. depth shows that there are no relationships between the oxygen isotopes with

depth. (e) The temperature profile from depth of 600-820 meters, showing measurements of homogenization fluid-inclusion temperatures for bladed calcites (blue), rhombic calcite crystal (orange) and quartz crystal of massive sample (purple).

Fig. 7. Plots of carbon and oxygen isotope values of calcite veins and scaling from outcrops and wells in the Chingshui geothermal field, showing data from this study and from Lu et al., (2017). Results show that calcites from outcrops and scales from wells IC-13 and IC-19 are end members in the system. Vein calcites from well IC-21 are widely distributed in between these end memers. The bladed calcites and most of the rhombic calcite crystals have lighter $\delta^{13}C$ and $\delta^{18}O$ values than those of massive calcites with/without quartz.

Fig. 8. Optical microscope images of fluid inclusions in the bladed calcite of R57-2(a) and rhombic calcite crystals of R127-3(b). The bladed calcite microscope image shows considerable variation of gas/liquid ratios in inclusions. Red arrow denotes a gas-rich inclusion while the blue arrow highlights a fluid-rich inclusion, which suggests that a relatively slight boiling occurred.

Fig. 9. The calculated $\delta^{18}O$ values of hot fluids associated with rhombic and bladed calcites are close to meteoric water mixing with steam condensed liquid, while the $\delta^{18}O$ values of fluids derived from massive calcite are much heavier than that of the local meteoric fluids. The latter may be mus temperatures of fluid inclusions in bladed and rhombic calcite, and clumped isotopic temperature for massive calcite.

us temperatures of fluid inclusions in bladed and rhombic calcite, and clumped isotopic temperature for massive calcite.

us temperatuus temperatures of fluid inclusions in bladed and rhombic calcite, and clumped isotopic temperature for massive calcite.

Fig.10. Relationships between $\delta^{18}O$ values of calcites and vein orientations. The lighter $\delta^{18}O$ values are predominantly distributed in the fracture orientation of N10-20˚E.

Fig.11. Three scenarios showing the fractures related to the framework of strike-slip faults assuming that N10~20˚E is the main orientation of geothermal conduits. They are (a) ~N10-20˚W, (b) ~N40-50˚E, and (c) co-existence of N10-20˚W and N40-50˚E.

Fig.12. Conceptual model of geothermal conduits in the Chingshui geothermal field. Two fault systems with orientations of N10-20˚W and N40-50˚E developed the main conduit with an orientation of N10-20˚E.

Table 1. Geochemical data of the composition of fluids sampled from wells

Table 2. Clumped isotope data and the calculated $\delta^{18}O$ VSMOW of parent fluids.

Table 3. Homogenization temperatures of fluid inclusions and the carbonate isotope values.

APPENDIX A. SUPPLEMENTARY DATA 1. Carbon and oxygen isotopic data

APPENDIX A. SUPPLEMENTARY DATA 2. Slaty cleavages measured at surface outcrop nearby the IC-21 drilling site in Chingshui geothermal area

APPENDIX A. SUPPLEMENTARY DATA 3.Fluid inclusion data

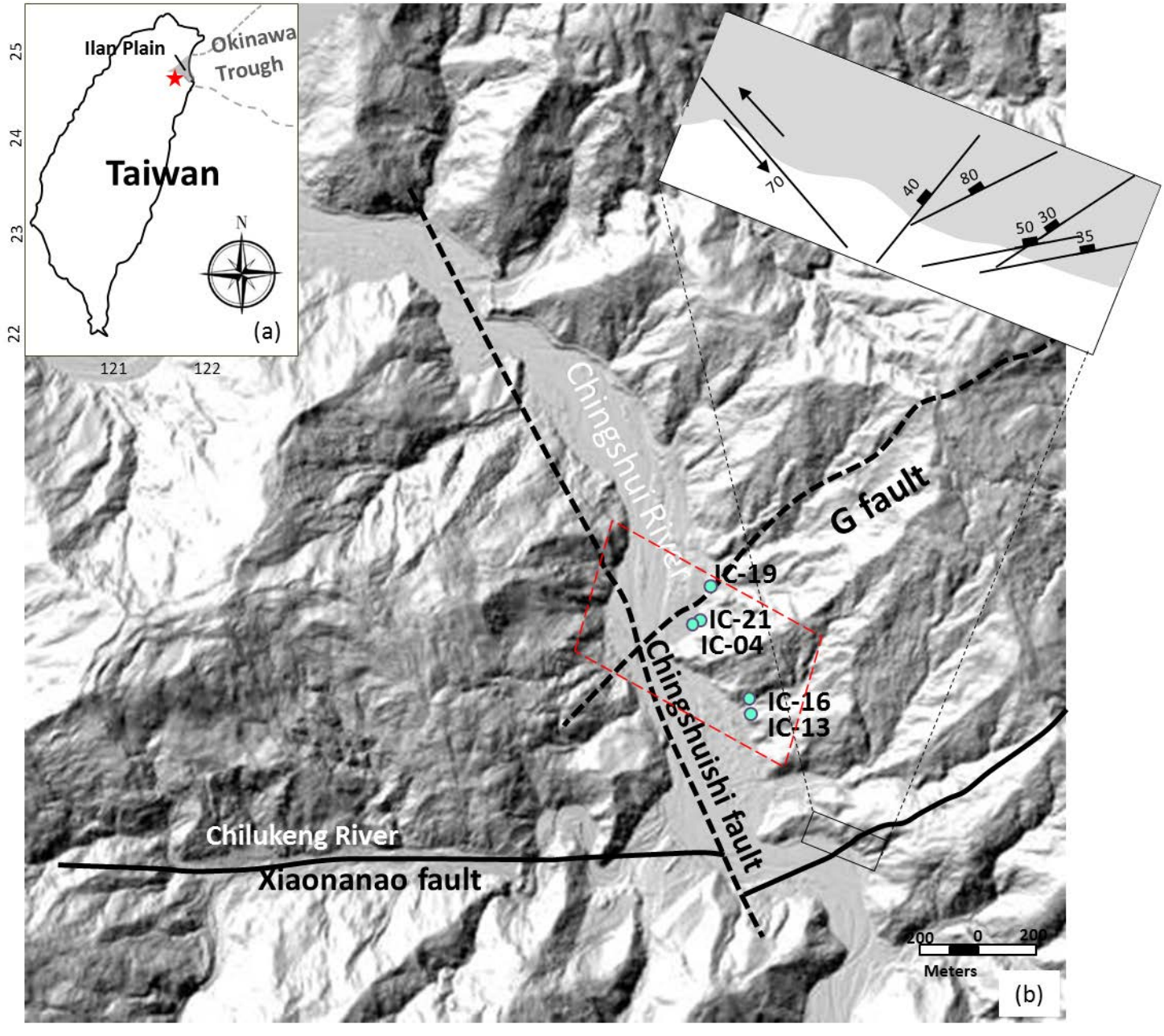
Ilan Plain
Okinawa Trough
Taiwan
N
(a)
25
24
23
22
121
122
70
40
80
50
30
35
Chingshui River
G fault
IC-19
IC-21
IC-04
IC-16
IC-13
Chingshuishi fault
Chilukeng River
Xiaonanao fault
200
0
200
Meters
(b)


(a)


(b)

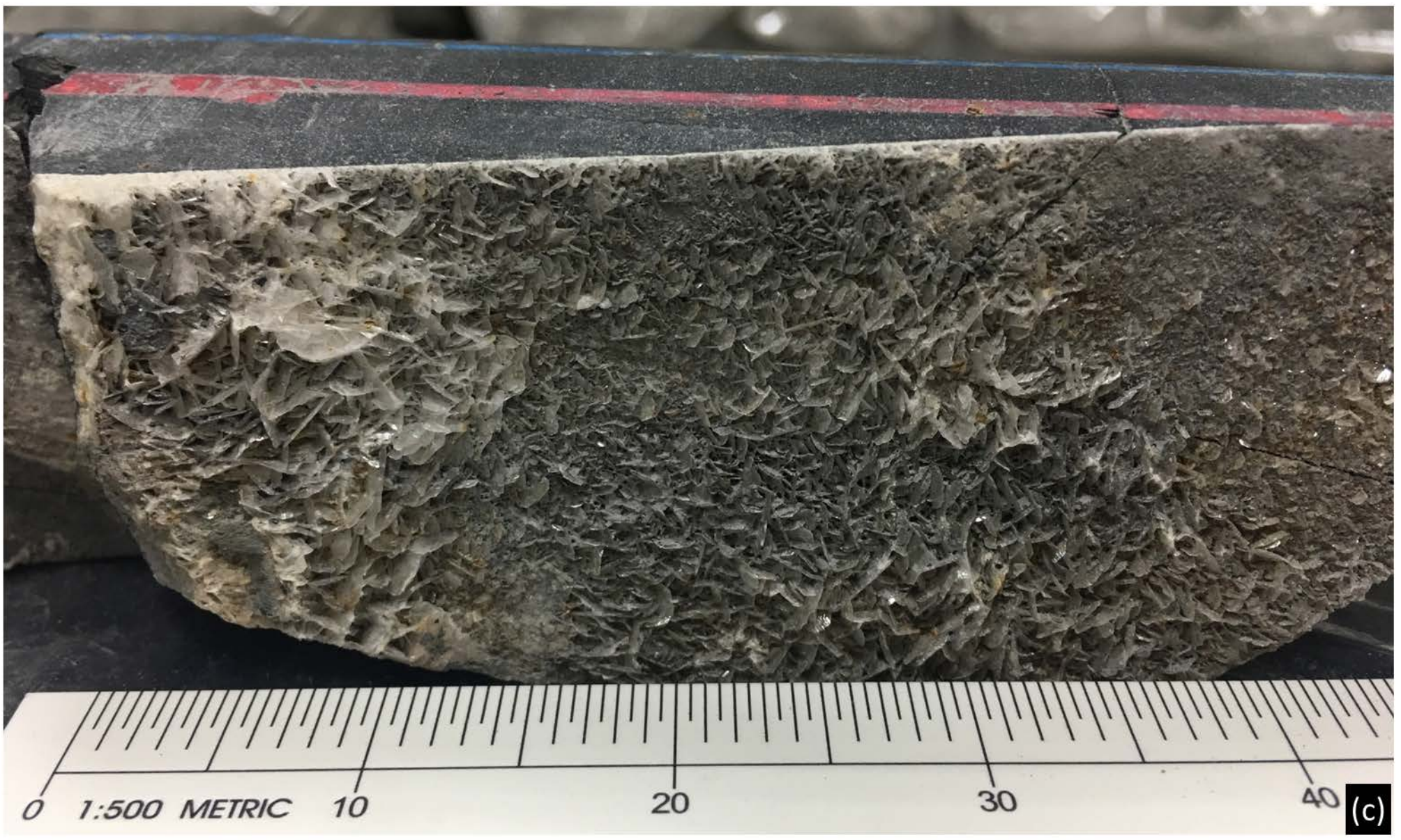
0
1:500 METRIC
10
20
30
40
(c)


(d)


(e)

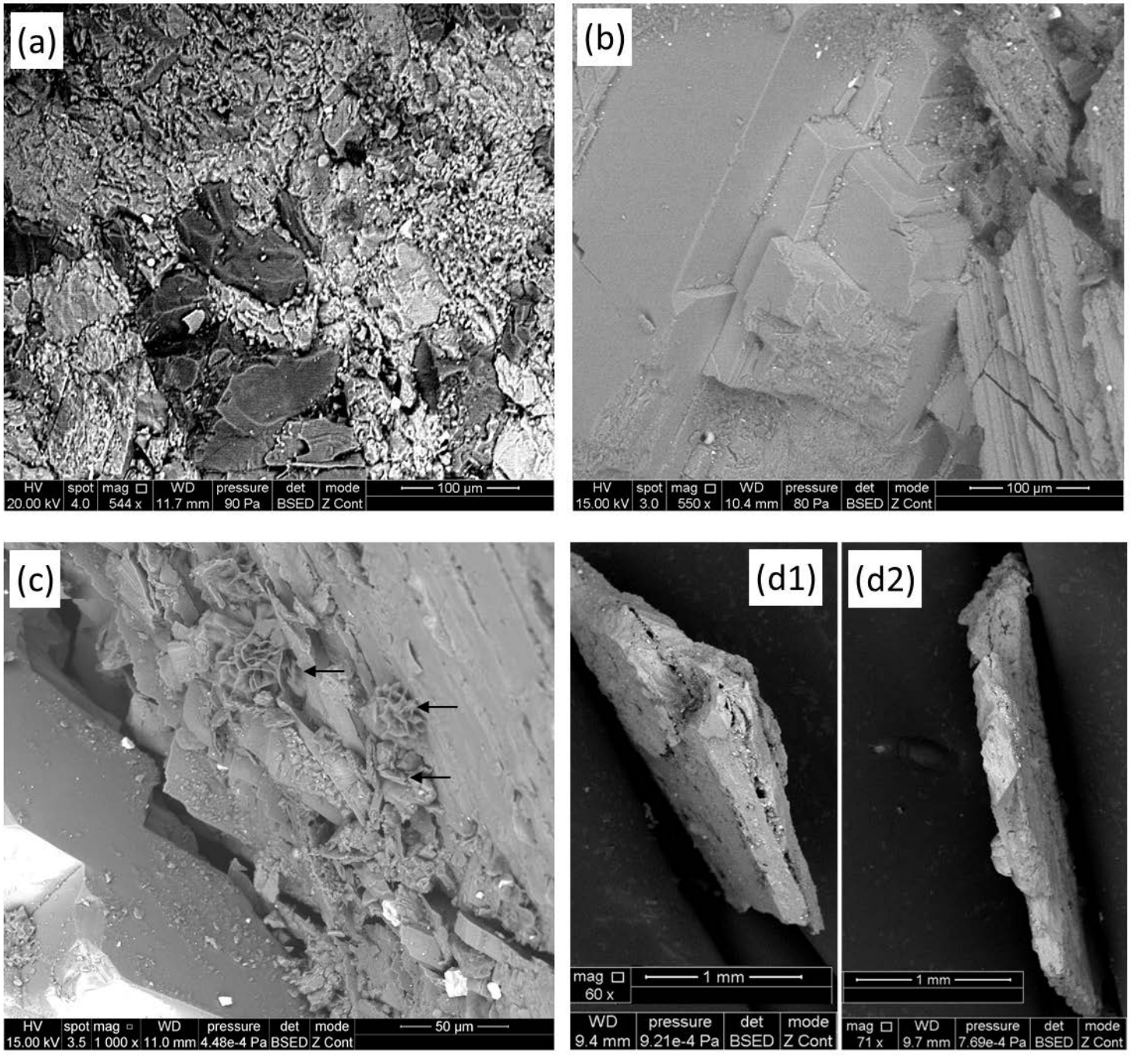
(a)
HV 20.00 kV
spot 4.0
mag 544 x
WD 11.7 mm
pressure 90 Pa
det BSED
mode Z Cont
100 µm
(b)
HV 15.00 kV
spot 3.0
mag 550 x
WD 10.4 mm
pressure 80 Pa
det BSED
mode Z Cont
100 µm
(c)
HV 15.00 kV
spot 3.5
mag 1 000 x
WD 11.0 mm
pressure 4.48e-4 Pa
det BSED
mode Z Cont
50 µm
(d1)
mag 60 x
1 mm
WD 9.4 mm
pressure 9.21e-4 Pa
det BSED
mode Z Cont
(d2)
1 mm
mag 71 x
WD 9.7 mm
pressure 7.69e-4 Pa
det BSED
mode Z Cont

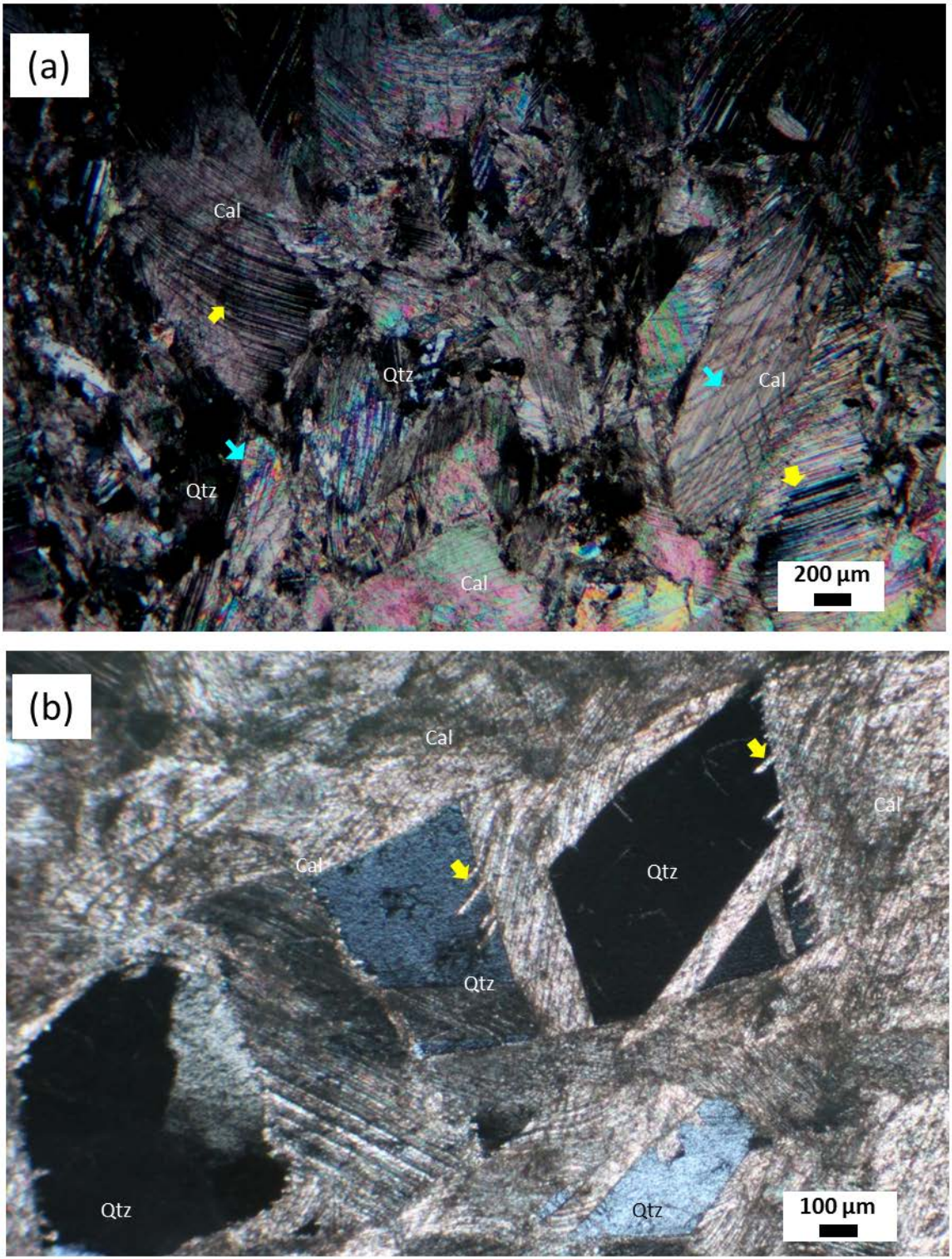
(a)
Cal
Qtz
Cal
Qtz
Cal
200 µm
(b)
Cal
Cal
Qtz
Cal
Qtz
Qtz
Qtz
100 µm

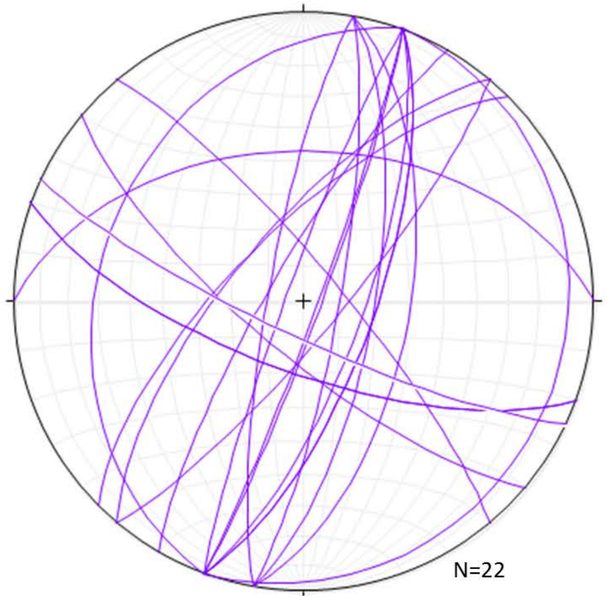

(a) Massive Calcite (With Quartz)

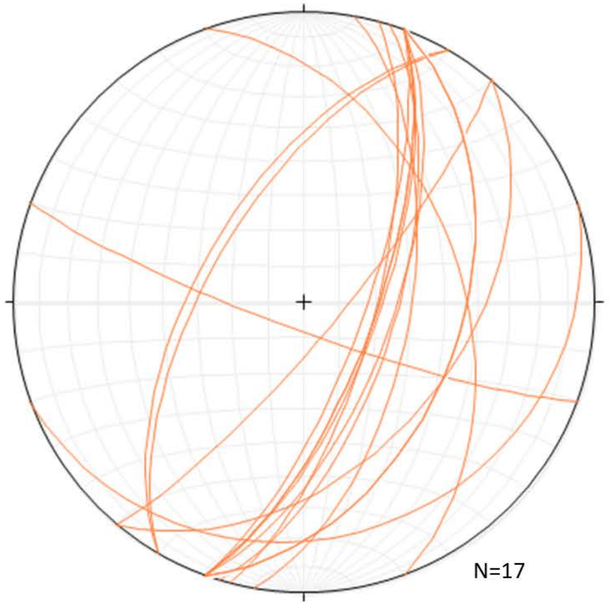

(b) Rhombic Calcite Crystal

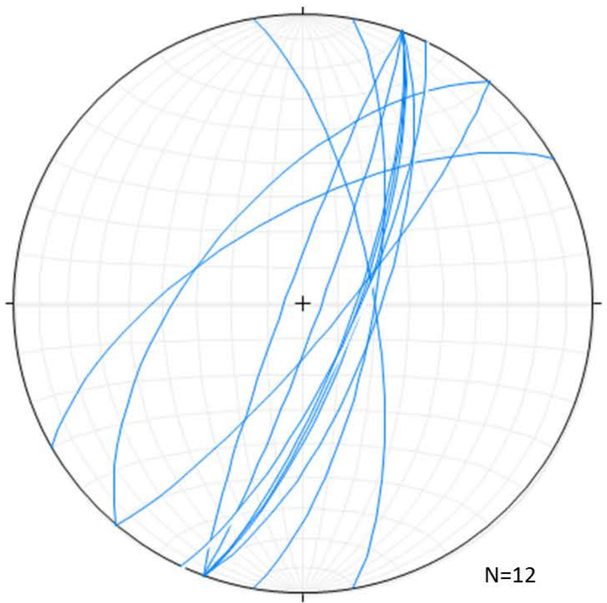

(c) Bladed Calcite

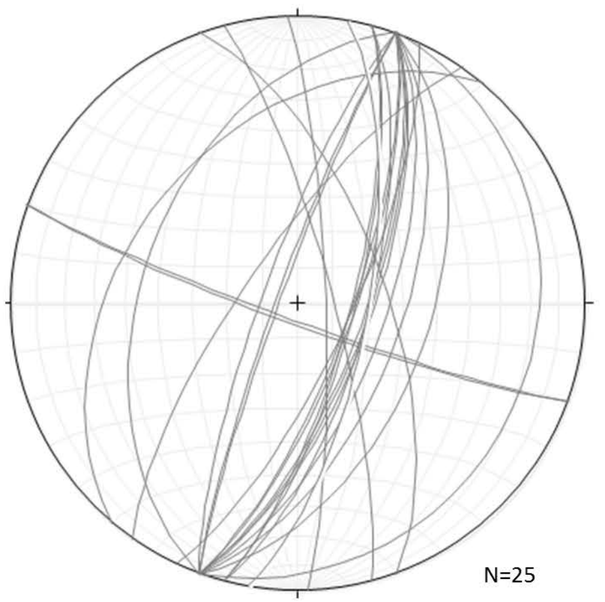

(d) Massive Calcite (Without Quartz)

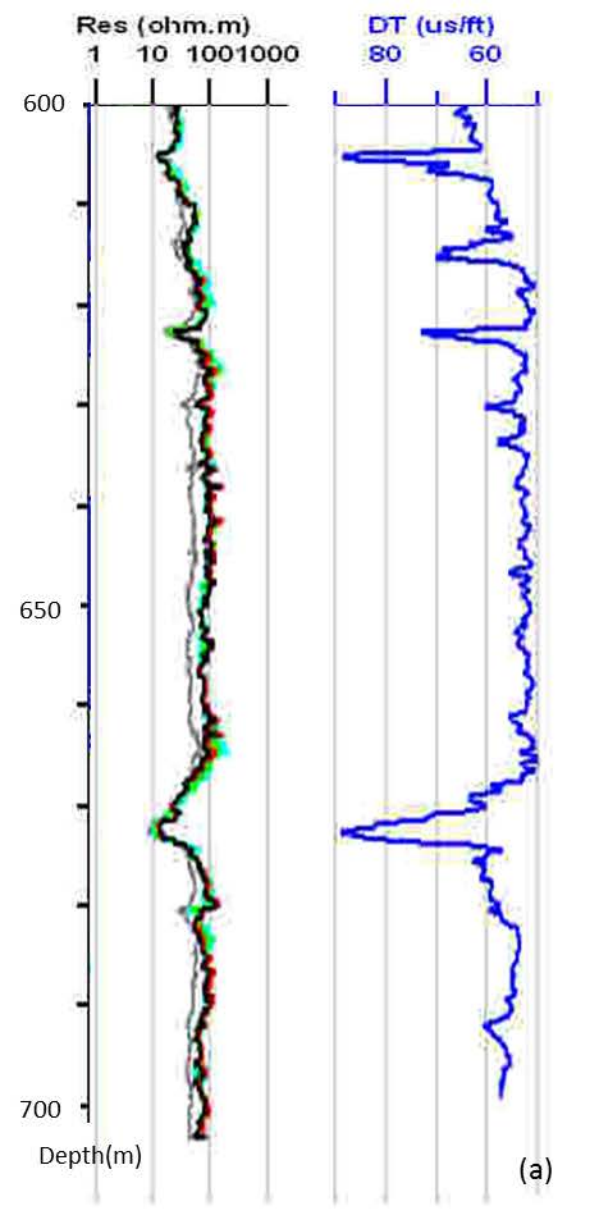
Res (ohm.m)
1 10 1001000
DT (us/ft)
80 60
600
650
700
Depth(m)
(a)

0
200
400
600
800
1000
1200
1400
100 120 140 160 180
Depth(m)
°C
(b)

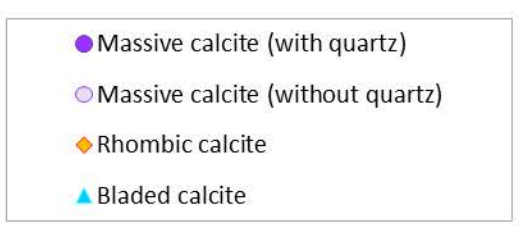
Massive calcite (with quartz)
Massive calcite (without quartz)
Rhombic calcite
Bladed calcite

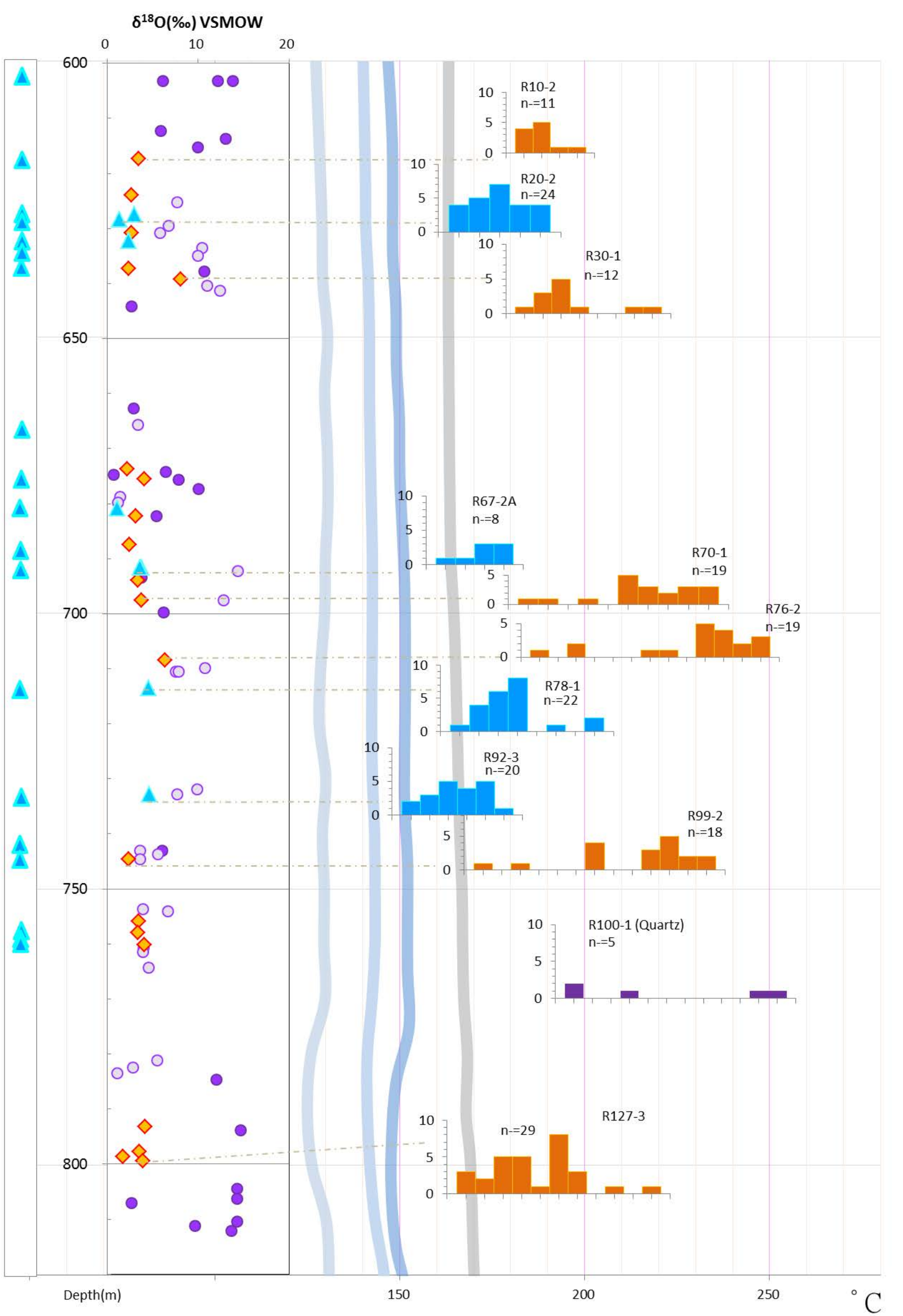
δ18O(‰) VSMOW
0 10 20
600
650
700
750
800
R10-2
n-=11
R20-2
n-=24
R30-1
n-=12
R67-2A
n-=8
R70-1
n-=19
R76-2
n-=19
R78-1
n-=22
R92-3
n-=20
R99-2
n-=18
R100-1 (Quartz)
n-=5
R127-3
n-=29
Depth(m)
150
200
250
°C

(c) (d) (e)

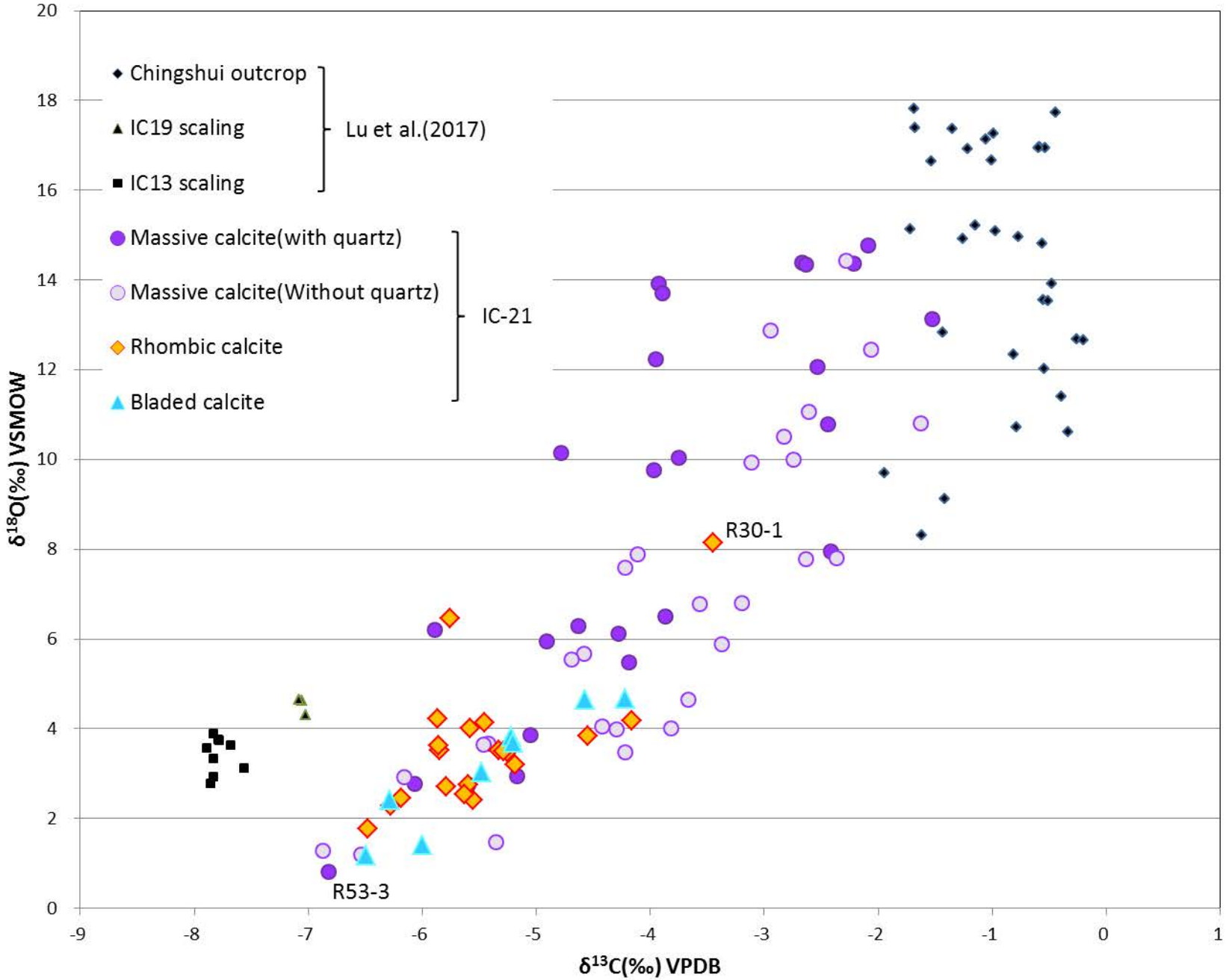
Chingshui outcrop
IC19 scaling
IC13 scaling
Lu et al.(2017)
Massive calcite(with quartz)
Massive calcite(Without quartz)
Rhombic calcite
Bladed calcite
IC-21
R30-1
R53-3
δ18O(‰) VSMOW
δ13C(‰) VPDB
20
18
16
14
12
10
8
6
4
2
0
-9
-8
-7
-6
-5
-4
-3
-2
-1
0
1

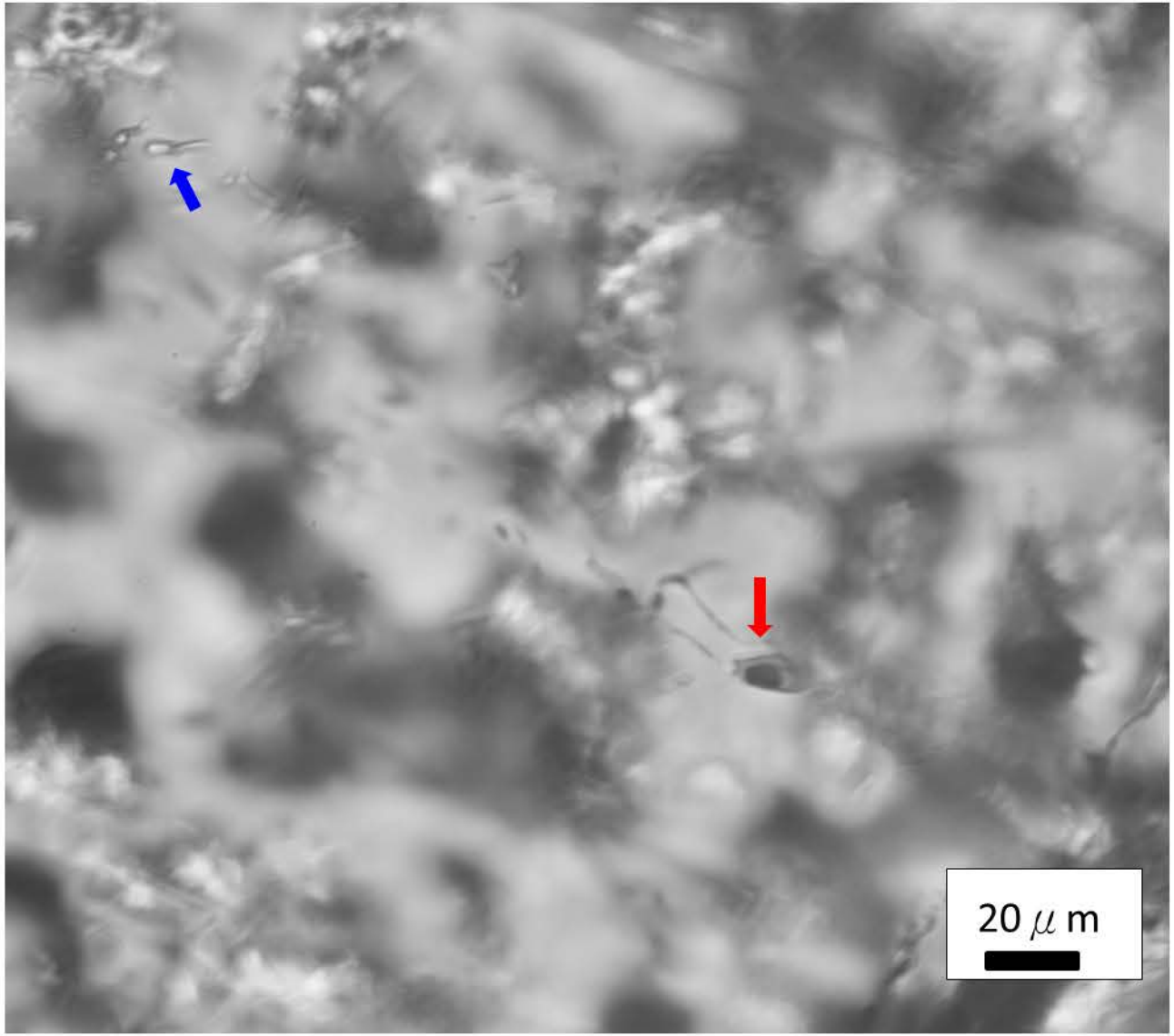
20 μ m

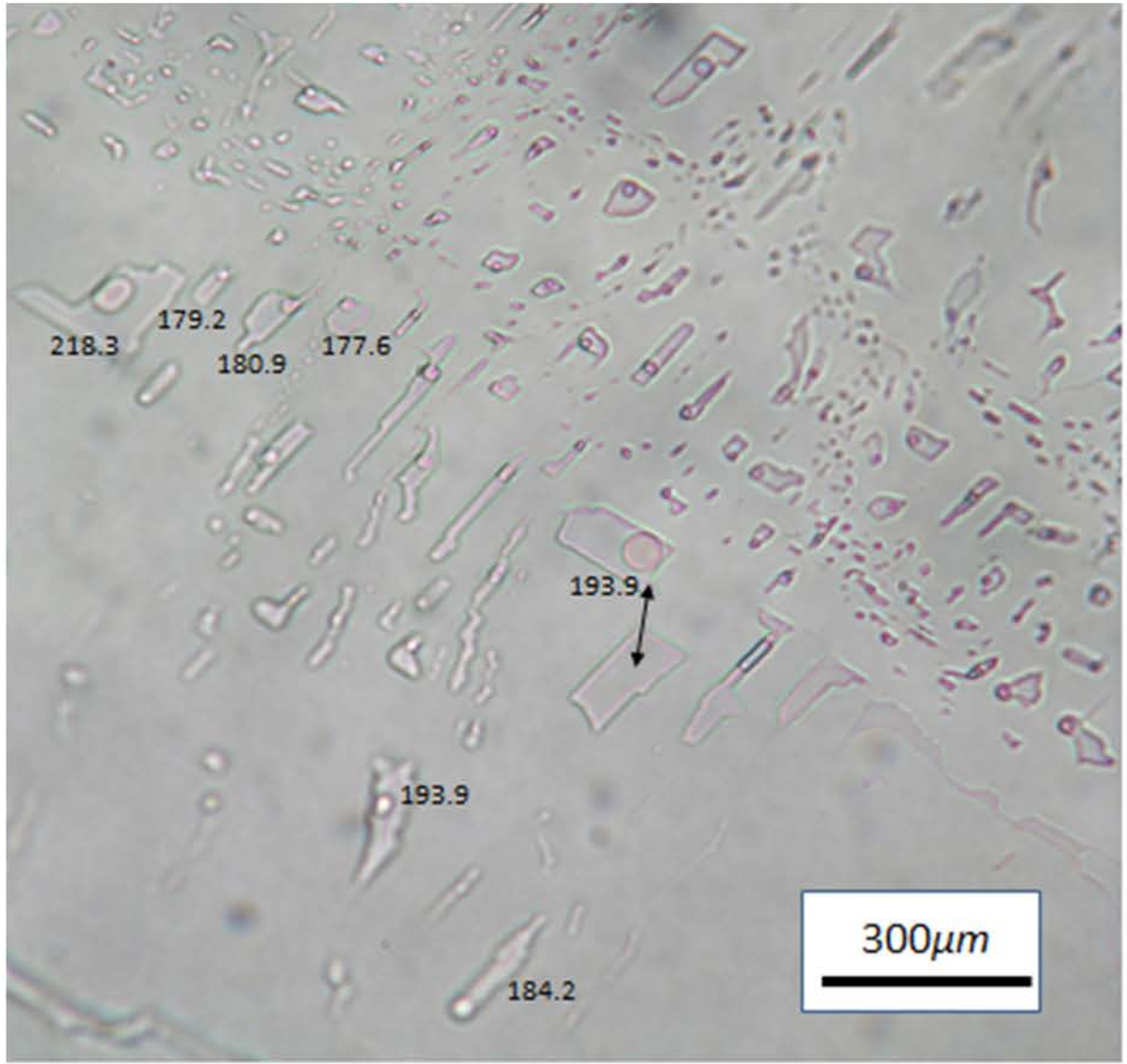
218.3
179.2
180.9
177.6
193.9
193.9
184.2
300μm

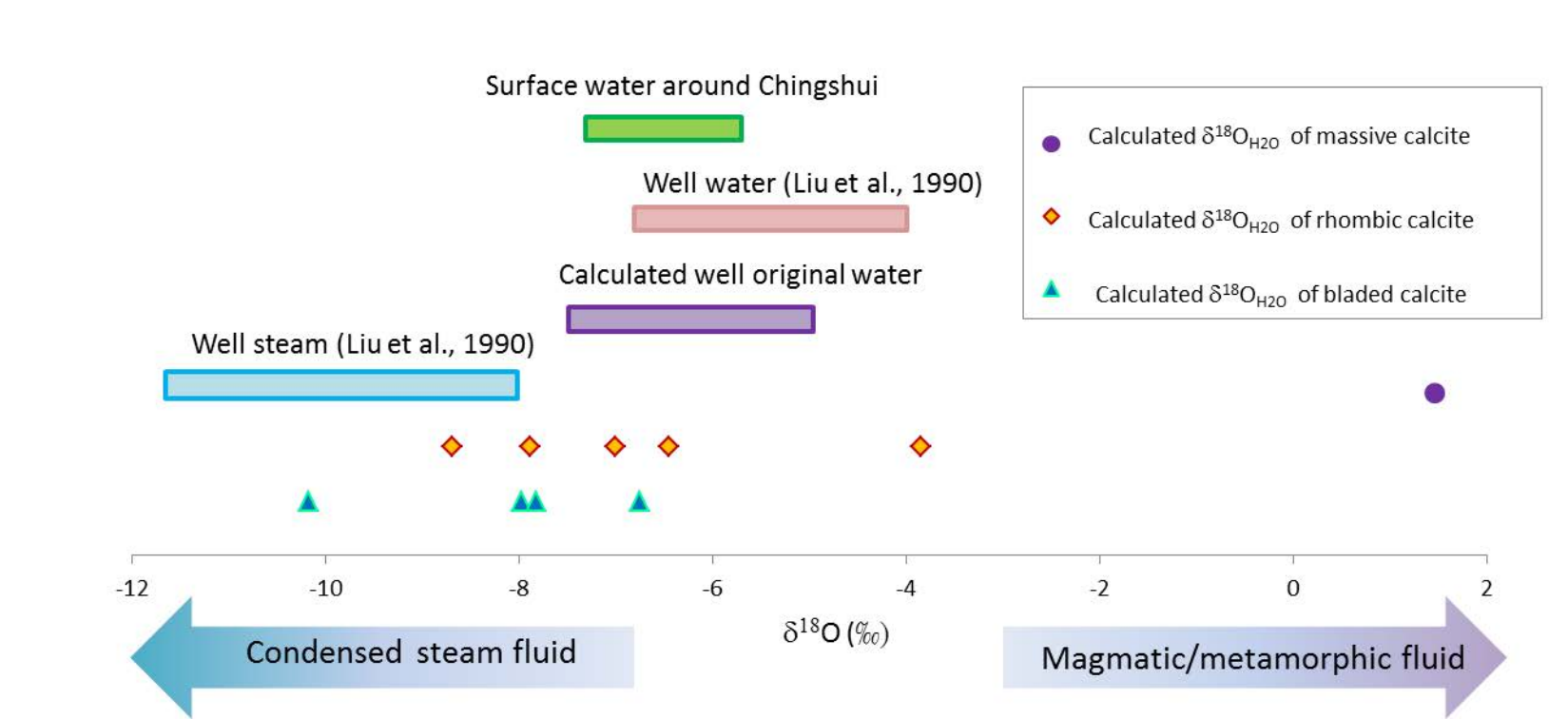
Surface water around Chingshui
Well water (Liu et al., 1990)
Calculated well original water
Well steam (Liu et al., 1990)
Calculated $\delta^{18}O_{H2O}$ of massive calcite
Calculated $\delta^{18}O_{H2O}$ of rhombic calcite
Calculated $\delta^{18}O_{H2O}$ of bladed calcite
-12
-10
-8
-6
-4
-2
0
2
$\delta^{18}O$ (‰)
Condensed steam fluid
Magmatic/metamorphic fluid

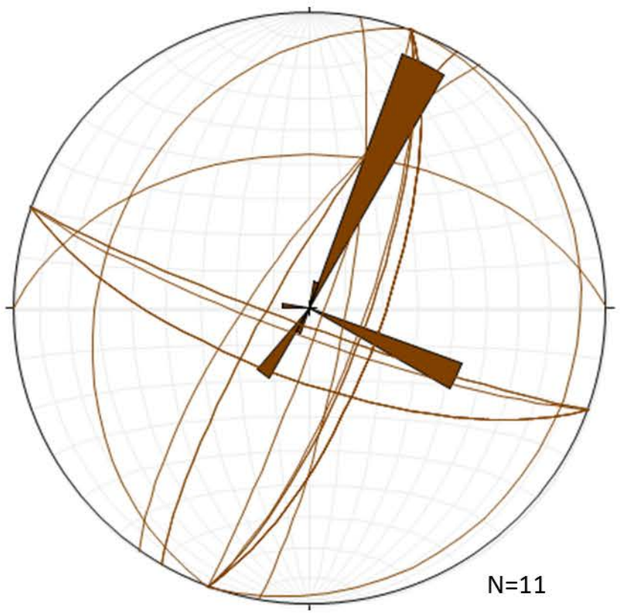

$\delta^{18}O$ values of calcite >10 ‰ VSMOW

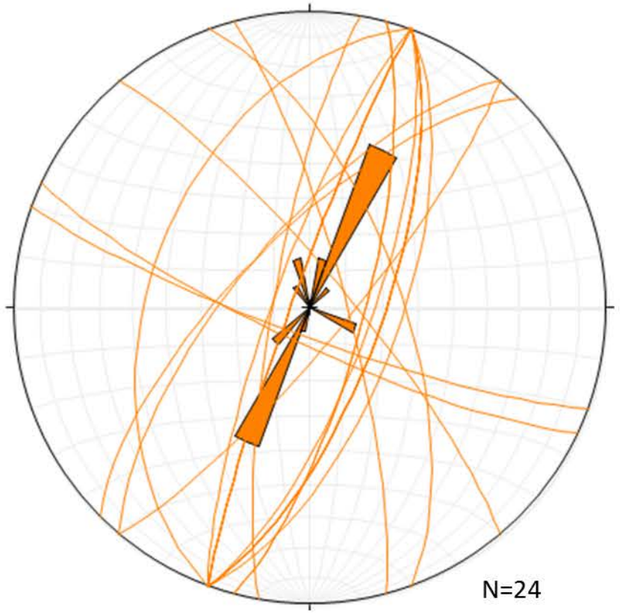

$\delta^{18}O$ values of calcite 5-10 ‰ VSMOW

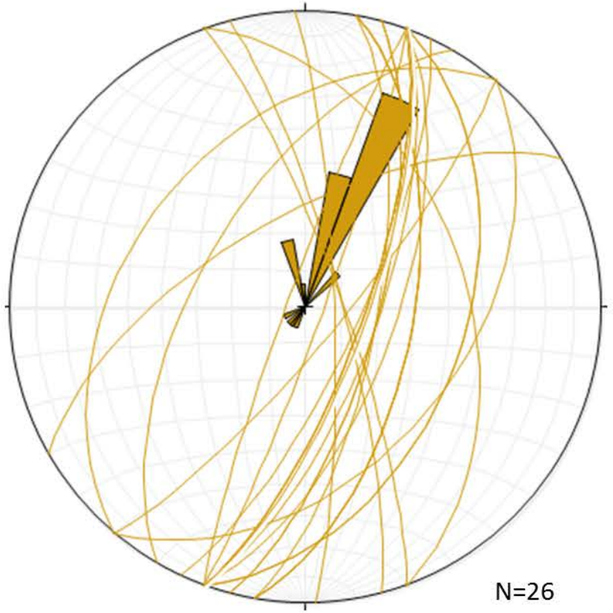

$\delta^{18}O$ values of calcite 3-5 ‰ VSMOW

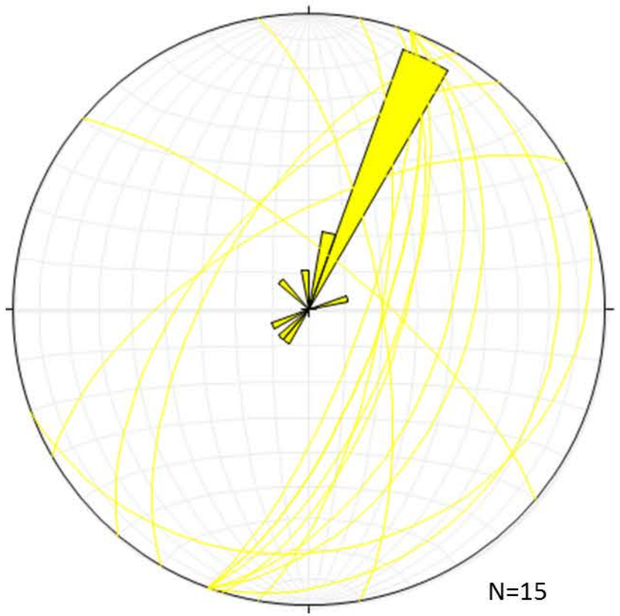

$\delta^{18}O$ values of calcite 0-3 ‰ VSMOW

magmatic fluid sources

Meteoric fluid sources

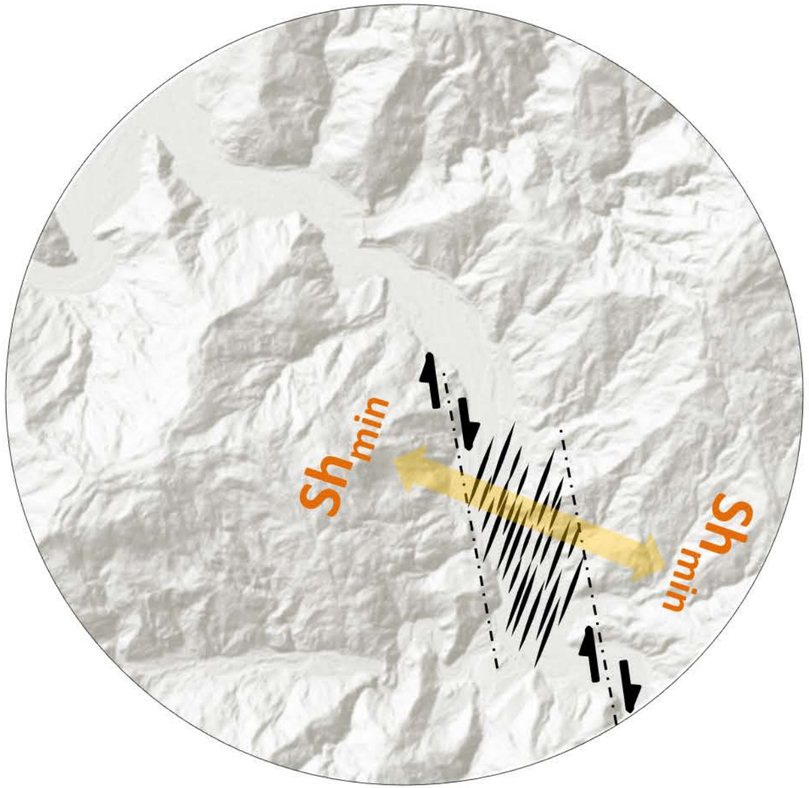

Model-A

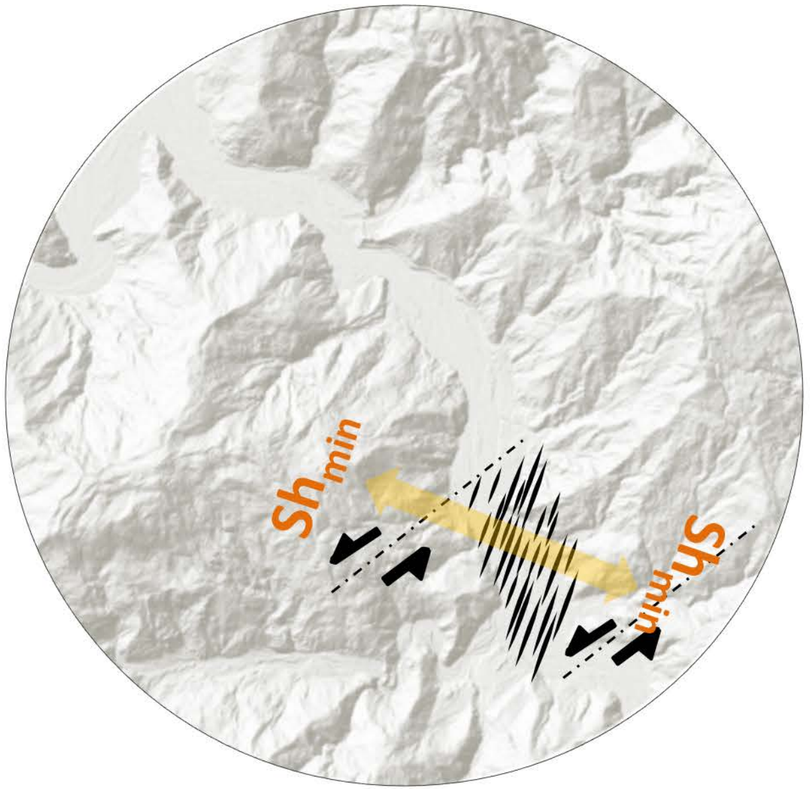

Model-B

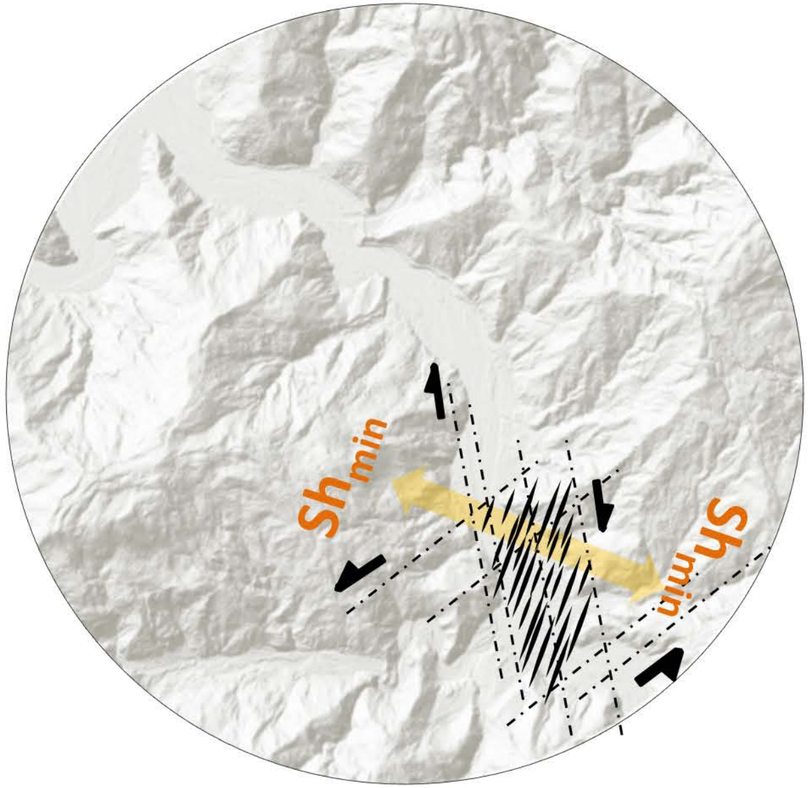

Model-A+B

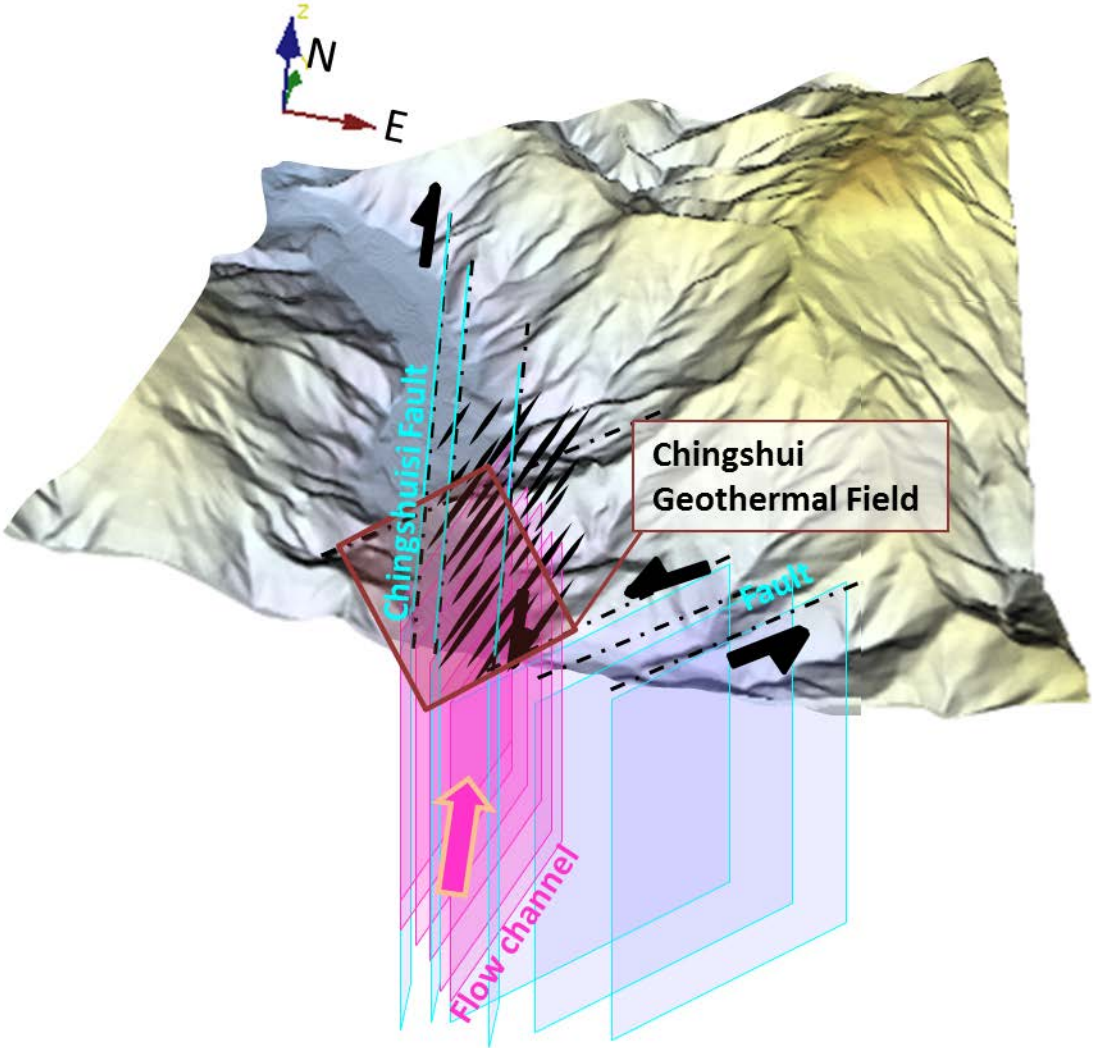
z
N
E
Chingshuisi Fault
Chingshui
Geothermal Field
Fault
Flow channel

Well No.	Buttom T (°C)	pH	HCO_3^- (ppm)	Cl^- (ppm)	SO_4^{2-} (ppm)	SiO_2 (ppm)	Na^+ (ppm)	K^+ (ppm)	Ca^{2+} (ppm)	Mg^{2+} (ppm)	B (ppm)	H_2O:NCG[c] (V%)	CO_2 in NCG (V%)
IC-04	201	8.8	2768	16	24	370	1149	36.0	1.0	0.8	31	-	-
IC-04	201	8.5	2619	18	32	342	1095	36.0	0.6	0.2	34	89.7 : 10.3	97.9
IC-21	175	9.0	1659	37	33	272	825	56.9	0.5	0	35	96.1 : 3.9	98.4
River	20	8.0	226			3.9	6.0	2.5	33	9.1	-	-	-

[a.] The The data of IC-04 are from Lin(2000) and Liu et al. (1990)

[b.] The The data of IC-21 are from ITRI (2012).

[c.] NCG means non-codensible gases.

	Replicates	$\delta^{13}C$	$\delta^{18}O$	$\delta^{18}O$	Ave Δ47	S.E.	T (˚ C)[a]			$d^{18}O_{H2O}$[b]
	(n)	(‰,VPDB)	(‰,SMOW)	(‰,VPDB)	(‰,CDES)	(‰,CDES)		Error-	Error +	(‰,SMOW)
R55-1	2	-4.3	10.6	-19.7	0.415	0.001	208	13	14	1.5
R76-2	3	-5.8	7.1 [c]	-23.1	0.442	0.005	173	15	16	-4.0 [d]

[a.] The calcite growth temperatures calculated from corrected D47 values are based on various theoretical and experimental calibrations derived by revised Kluge et al.(2015).

[b.] The $\delta^{18}O$ of fluids were estimated by Friedman & O'Neil (1977)

[c.] The $\delta^{18}O$ value is 7.1 ‰ VSMOW simultaneously measurement with clumped isotope, little higher than oxygen isotopic value of 6.5‰.

[d.] If the δ18O value of calcite is 6.5 ‰ VSMOW, then the $d^{18}O$ H_2O will be -4.6 ‰ VSMOW.

crystal forms	sample name	depth (m)	$\delta^{13}C$(‰) VPDB	$\delta^{13}C$ std.	$\delta^{18}O$(‰) VSMOW	$\delta^{18}O$ std.	Strike	Dip	TH of fluid inclusions(°C)	Calculated fluid value$\delta^{18}O$ (‰) VSMOW
Rhombic calcite crystal	R10-2	617.40	-5.8	0.01	3.5	0.02	210	60W	182-197	-7.0
Rhombic calcite crystal	R30-1C	639.25	-3.4	0.01	8.1	0.02	290	82S	184-216	-2.3
Rhombic calcite crystal	R70-1C	697.50	-4.5	0.01	3.8	0.02	20	70E	186-231	-6.5
Rhombic calcite crystal	R76-2	708.44	-5.8	0.02	6.5	0.02	20	70E	186-246	-3.8
Rhombic calcite crystal	R99-2C	744.59	-6.2	0.01	2.4	0.01	Hydrothermal breccia		172-235	-8.7
Rhombic calcite crystal	R127-3	797.73	-5.9	0.01	3.6	0.02	340	45E	166-218	-7.9
bladed calcite	R20-2C	628.37	-6.0	0.01	1.4	0.01	240	65W	165-189	-10.2
bladed calcite	R67-2A	691.65	-5.2	0.01	3.8	0.01	20	74E	162-179	-8.0
bladed calcite	R78-1	713.47	-4.6	0.00	4.6	0.01	20	85E	168-201	-6.8
Platy calcite	R92-3C	732.87	-4.2	0.00	4.7	0.04	200	85W	152-178	-7.8
Quartz	R100-1	745.70	-	-	-	-	80	55E	179-254	